Economic Geology, v. 114, no. 2, pp. 353–373

Sulfur Isotopes in Biogenically and Abiogenically Derived Uranium Roll-Front Deposits

Gretchen Hough,[1] Susan Swapp,[1,†] Carol Frost,[1] and Mostafa Fayek[2]

[1]*University of Wyoming, Department of Geology and Geophysics, 1000 E. University Ave., Laramie, Wyoming 82071*

[2]*University of Manitoba, Department of Geological Sciences, 240 Wallace Building, 125 Dysart Rd., Winnipeg, Manitoba R3T 2N2, Canada*

Abstract

Ore assemblages in uranium roll-front deposits are highly variable and heavily dependent on Eh/pH conditions. Sulfur isotopes in pyrite traditionally have been employed to distinguish between biogenic or abiogenic redox pathways as drivers of roll-front propagation. However, the extent of and constraints on bacterial productivity have never been quantified, nor have the chemical conditions imposed by either primary formation mechanism. Moreover, this approach implicitly assumes that deposits form via one process or the other and disregards the possibility that both processes participate simultaneously in generating some orebodies. In this study, we analyzed sulfur isotopes from pyrite coprecipitated with uranium in two Wyoming roll-front deposits: Lost Creek and Willow Creek Mine Unit 10. The results document contrasting isotopic fractionation that correlates with pyrite morphology. Both deposits evolved with both abiogenic and biogenic redox mechanisms as active contributors to ore formation. In the past, bimodal fractionation behavior with pyrite morphology has been attributed to distinct temporal episodes of pyrite formation, driven by either a change in redox mechanism or multiple independent fluid events with unique isotopic signatures. However, neither explanation is appropriate for the isotopic trends identified in this study, where the two pyrite morphologies appear coeval in both deposits. Moreover, the contemporaneous formation of both pyrite morphologies cannot occur under the same conditions by the same precipitation mechanism because of the difference in their free energies of formation. The data suggest a third alternative in which pyrite morphology correlates to its biogenic or abiogenic mode of formation. Given the isotopic composition of pre-ore pyrite, sulfur isotope fractionation trends within the ore zone can be applied to establish prolificacy of bacteria and chemical conditions of the ore-forming solution.

In both study sites, framboidal pyrite occurred as the primary by-product of sulfur-reducing bacteria, and the corresponding fractionation pattern constrains the sulfur availability and bacterial productivity. Euhedral to anhedral pyrite precipitated from abiogenic redox, the sulfur fractionation recording Eh/pH gradients during ore evolution. At Lost Creek, framboidal pyrite produced $\delta^{34}S$ values from –50.8 ± 0.5‰ to +142.8 ± 0.3‰, while subhedral pyrite ranged from –68.1 ± 0.4‰ to +33.8 ± 0.3‰ with $\delta^{34}S$ values increasing toward the barren, unaltered contact. Pre-ore pyrite at Lost Creek ranged from –0.8 ± 0.5‰ to +70.6 ± 0.3‰. $\delta^{34}S$ values from biogenically derived pyrite at Lost Creek indicate a closed system with limited sulfate availability and a slow rate of bacterial reduction, implying restricted bacterial activity. Abiogenic fractionation behavior indicates a system driven by an Eh drop under neutral or basic pH conditions, and pyrite distribution across the roll identifies abiogenic pyrite recycling as the dominant redox mechanism at Lost Creek. At Willow Creek Mine Unit 10, framboidal pyrite ranged from –32.5 ± 0.4‰ to +68.2 ± 0.4‰, and subhedral pyrite ranged from –45.1 ± 0.4‰ to +5.4 ± 0.4‰. The subhedral pyrite $\delta^{34}S$ values initially increased into the center of the roll and subsequently decreased again approaching the barren, unaltered contact. Pre-ore pyrite ranged from –48.1 ± 0.4‰ to +15.6 ± 0.5‰. Willow Creek Mine Unit 10 biogenically produced $\delta^{34}S$ values show minimal fractionation from pre-ore pyrite, indicating an open system with abundant sulfate and rapid reduction from prolific bacterial activity. The abiogenic trends indicate an Eh drop and low pH at the barren, altered contact progressively neutralized across the orebody. This correlates to the anticipated Eh/pH gradients in a system dominated by biogenic redox.

Introduction

Project relevance

Uranium in roll-front deposits has been recovered through in situ techniques for decades, but this mining method has had varied success because of an inability to anticipate uranium mineralogy. Uraninite (UO_2) and coffinite ($U(SiO_4)_{1-x}(OH)_{4x}$) hosting tetravalent uranium are common uranium minerals found in roll-front deposits; however, some roll-front deposits are dominated by carnotite group minerals ($K_2(UO_2)_2(VO_4)_2 \cdot 3H_2O$) that host hexavalent uranium and pentavalent vanadium and are comparatively insoluble in oxidizing lixiviants (Langmuir, 1978; Finch and Murakami, 1999; Stewart et al., 2000; Nye, 2015). The variations in ore assemblages in roll-front deposits reflect differences in aqueous geochemistry (Langmuir, 1978; Zhil'tsova et al., 1982, 1990; Drever, 1997; Finch and Murakami, 1999; Stewart et al., 2000). Given their effect on uranium mineralogy, it is critical to understand the conditions of formation and potential controls on system chemistry, an aspect of deposit characterization that still remains largely undefined.

The co-occurrence of pyrite and uranium mineralization in roll-front deposition identifies pyrite as a key constituent in system redox. Where uranium precipitates as a consequence of localized reducing conditions, the redox potential established through pyrite cycling is responsible for generating the redox interface that drives ore formation. This pyrite recycling process may be propagated through biogenic or abiogenic mechanisms (Granger and Warren, 1969; Rackley, 1972). Sulfur isotopes from pyrite have been employed successfully as

† Corresponding author: email, swapp@uwyo.edu

ISSN 0361-0128; doi: 10.5382/econgeo.2019.4634; 21 p.
Digital appendices are available in the online Supplements section.

Submitted: April 28, 2017
Accepted: January 7, 2019

a redox proxy to establish the dominance of either abiogenic or biogenic redox within roll-front deposits. However, the extent of and constraints on bacterial productivity have never been quantified, nor have the chemical conditions imposed by either primary formation mechanism. This study advances the use of pyrite as a redox proxy by utilizing spatial sulfur isotope trends to constrain the prolificacy of bacterial activity and Eh/pH gradients established during ore formation. We examine sulfur isotope composition ($^{34}S/^{32}S$) in pyrite from two Wyoming roll-front deposits to determine the extent of each redox mechanism and the corresponding influences on chemical conditions.

Redox mechanisms

In a roll front controlled by bacteria, the redox interface is established between ferro-oxidizing and sulfur-reducing bacteria (SRB) that generate sulfate through pyrite oxidation and drive reprecipitation of ore zone pyrite through sulfate reduction, respectively (Fig. 1). Because there is sulfur available for bacterial reduction from preexisting pyrite, organic material, and aqueous sulfate in the groundwater, pyrite may be concentrated within the orebody of a biogenically propagated roll front, given a highly productive SRB population (Rackley, 1972). Even more significant are the chemical conditions that may be established in a prolific bacterial system. Ferro-oxidizing bacteria function at a pH between 2 and 4 with an established Eh of up to 760 mV (Kuznetsov et al., 1963; Rackley, 1972); SRB exist at near-neutral pH of about 7.8 to 8.4 and generate an Eh of –200 mV (Jones and Starkey, 1962; Rackley, 1972).

The abiogenic redox model is similarly dependent on pyrite recycling (Fig. 2); however, because sulfate is typically kinetically inert at low temperatures, roll-front propagation occurs through intermediate sulfur species (Granger and Warren, 1969; Brunner and Bernasconi, 2005). Under semi-oxic conditions, fluids migrating down gradient will cause intermediate oxidation of pyrite, generating several metastable sulfur species such as thiosulfate ($S_2O_3^{2-}$) and sulfite (SO_3^{2-}) that will disproportionate into H_2S and sulfate. The sulfate is chemically inert and flows out with the groundwater, and the H_2S produces ore zone pyrite (Granger and Warren, 1969; Brunner and Bernasconi, 2005). Unlike the biogenic model, the continuous removal of sulfate through abiogenic redox will deplete ore zone pyrite, decreasing the quantity of pyrite within the roll front compared to the barren, unaltered sandstone beyond the orebody. Additionally, the abiogenic pyrite recycling process will exert different influences on the ore-forming solution compared to Eh/pH gradients predicted for biogenic redox. Eh decreases across the orebody in both biogenic and abiogenic redox models; however, H^+ is generated at each stage in the abiogenic redox process (Fig. 2), which has the potential to drive down system pH and maintain highly acidic conditions across the roll in contrast to the biogenic model.

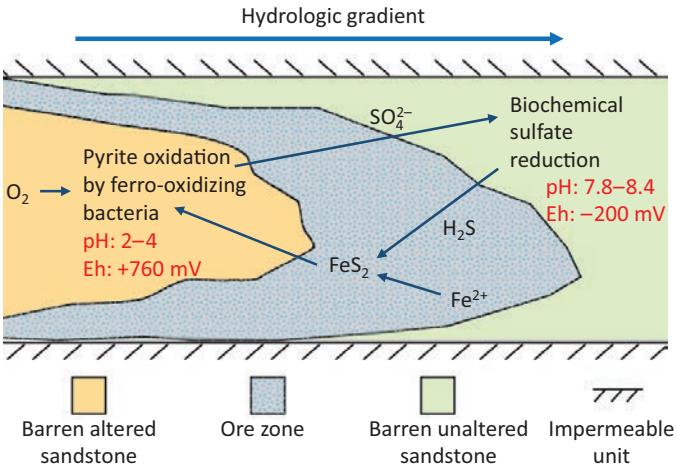

Fig. 1. Biogenic redox model (adapted from Rackley, 1972). The redox interface is established between ferro-oxidizing bacteria in the barren, altered sandstone and sulfur-reducing bacteria (SRB) in the barren, unaltered sandstone. Ferro-oxidizing bacteria oxidize pyrite and produce sulfate that is flushed across the roll with groundwater. SRB reduce sulfate and generate H_2S, which drives reprecipitation of ore zone pyrite. An Eh gradient is established across the ore zone from +760 to –200 mV, and a pH gradient from pH 2 to 4 to pH 8 (Jones and Starkey, 1962; Kuznetsov et al., 1963; Rackley, 1972).

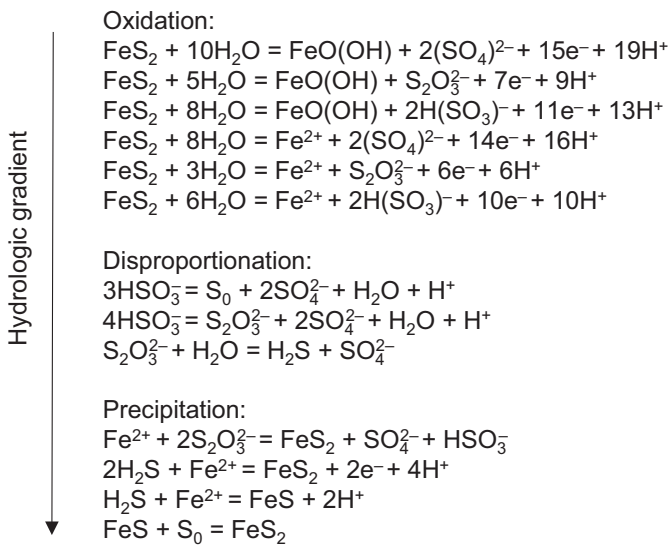

Fig. 2. Abiogenic redox model delineating step-wise chemical reactions in neutral to acidic pH (adapted from Granger and Warren, 1969). Hydrologic gradient indicates fluid flow from barren, altered sandstone through the ore horizon. H^+ is generated throughout the pyrite recycling process, which drives down system pH.

Sulfur isotopes in roll-front deposits: Results from previous studies

Before recent technological advancements that have allowed for in situ grain sampling, pyrite from roll-front deposits was characterized through bulk sulfur analyses. No previous studies report sulfur isotope analyses of sulfides from Lost Creek and Willow Creek Mine Unit 10, but sulfur isotope data are available for sulfide mineral separates from other sandstone-hosted roll-front uranium deposits in Wyoming. A large range of $\delta^{34}S$ values was obtained for pyrite from the Gas Hills uranium district, from –52 to +10‰ (Jensen, 1958; Cheney and Jensen, 1966). Warren (1972) documented a similar range in $\delta^{34}S$ values of –33 to +19‰ from pyrite from the Shirley Basin uranium district. A single analysis of pyrite from the Hauber

uranium deposit in the Powder River Basin yielded $\delta^{34}S$ = –49‰ (Bullock and Parnell, 2017). Jensen (1958) interpreted the sulfur isotope data to suggest a biogenic origin for sulfide, but Warren (1972) interpreted a similar range in $\delta^{34}S$ values to argue in favor of an abiogenic process. Bullock and Parnell (2017) considered sulfur isotope data from these and other roll-front deposits along with pyrite zones in sandstones adjacent to mud rock and concluded that the ^{34}S-depleted isotopic compositions were consistent with the involvement of microbial activity.

Although bulk sulfur isotope analyses precluded the separate isotopic measurements of temporally and morphologically distinct phases of pyrite within deposits, it still allowed for spatial examination of isotopic trends across deposits. In one comprehensive study of four Texas roll fronts, Reynolds et al. (1982) identified several key characteristics distinguishing biogenically and abiogenically derived deposits. In the biogenically controlled roll front, there was substantial organic material dispersed throughout the host rock and no apparent concentration of pyrite at the redox boundary (it was instead randomly distributed throughout the deposit), and sulfur isotopes within the roll varied from –34 to +16‰, spanning a range both lower and higher than pre-ore pyrite, which measured from –20 to 0‰. In contrast, what were characterized as abiogenically derived deposits were noted to have very little or no observable carbonaceous debris, a systematic decrease in the amount of pyrite across the orebody with the greatest concentration in the barren, unaltered core ahead of the roll, and sulfur isotope values ranging from –47 to –26‰, lighter than both the biogenic deposit and pre-ore values.

In a recent study utilizing in situ techniques for a South Australian roll front, Ingham et al. (2014) reported a range in $\delta^{34}S$ values of –43.8 to +32.4‰ and found that they could be divided into two morphologically distinct groupings: framboidal pyrite produced values from –43.8 to –18.3‰, and cubic pyrite, cements, and porous overgrowths showed a much broader range ($\Delta^{34}S$ > 65‰) and were typically heavier (up to 32.4‰). The framboidal pyrite and the lumped cubic pyrite, cements, and porous overgrowths formed in two distinct temporal episodes, and the isotopic heterogeneity was interpreted as two separate ore-forming fluid events with different isotopic signatures. In another study of a Nebraska roll front, framboidal pyrite $\delta^{34}S$ values ranged from –35.9 to –20.7‰, and subhedral pyrite values from –51.7 to –23.1‰. Both morphologies were attributed to biogenic redox due to the extreme ^{34}S depletion. A third, unspecified morphological type produced a range from –13.3 to –5.0‰ attributed to abiogenic processes due to the higher $\delta^{34}S$ values (Meek, 2014). Although this categorical grouping of pyrite by isotopic range regardless of morphology to identify redox mechanism is prevalent in literature (Jensen, 1958; Cheney and Jensen, 1966; Leibold, 2013; Meek, 2014; Bonnetti et al., 2015), it may be an invalid approach given the isotopic trends anticipated as a result of biogenic and abiogenic processes, as outlined below. Additionally, it is scope-limiting for the information that can be extracted from sulfur isotope analyses for deposit characterization if biogenic and abiogenic influences can be dissected and measured separately regardless of the dominant redox mechanism, as we will establish.

Predicted biogenic and abiogenic isotopic trends

Biogenic and abiogenic redox mechanisms are controlled by different variables in roll-front deposits and will record unique sulfur isotope signatures. The bond strength of ^{34}S-O is greater than that of ^{32}S-O. Because of this physical characteristic, sulfur oxides such as sulfate preferentially incorporate ^{34}S, giving them high $\delta^{34}S$ values and leaving sulfides ^{34}S depleted regardless of their biogenic or abiogenic derivation (Sakai, 1957, 1968; Ohmoto, 1972; Seal, 2006). SRB naturally capitalize on the weaker bond strength of ^{32}S-O during the reduction process, more readily metabolizing ^{32}S to produce pyrite with lower $\delta^{34}S$ values than original sulfate (Harrison and Thode, 1958; Nakai and Jensen, 1964; Brüchert, 2004; Seal, 2006). However, the final fractionation value from biogenic sulfate reduction is dependent on the rate of reduction (Gomes et al., 2017) and fraction of available sulfate processed (Fig. 3), making it possible to directly assess the prolificacy of SRB in a roll front with the sulfur isotope signatures recorded in biogenically generated pyrite. In a closed system where a large percentage of available sulfate is reduced, the bulk $\delta^{34}S$ values of ore zone pyrite will approach the original $\delta^{34}S$ value of the sulfate. However, individual grains precipitated in a closed system may exhibit Rayleigh fractionation, varying greatly from the bulk sulfur isotope composition (Ohmoto and Goldhaber, 1997; Seal et al., 2000; Seal, 2006; Gomes et al., 2017). In contrast, if biogenic reduction is occurring at a rapid rate, fractionation from the bulk isotopic composition will be limited (Harrison and Thode, 1958; Kaplan and

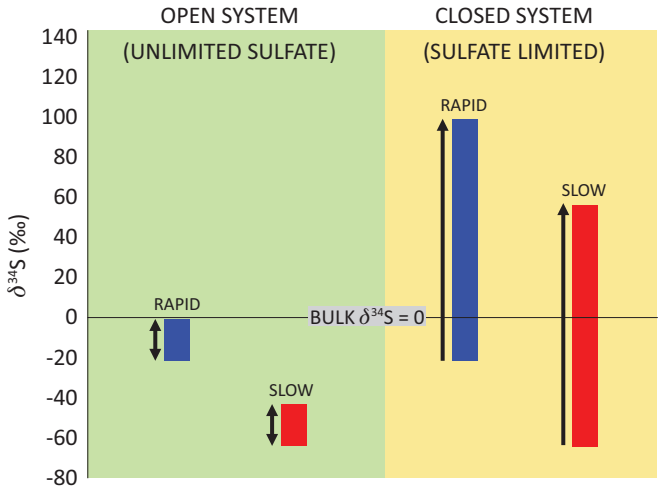

Fig. 3. The effect of bacterial reduction rate and sulfur availability on sulfur isotope fractionation behavior. Initial bulk sulfur pool $\delta^{34}S$ = 0‰. In an open system with unlimited sulfate (green field), variation of $\delta^{34}S$ values is minimal. Under conditions of rapid biogenic redox (blue bar), $\delta^{34}S$ values are similar to the $\delta^{34}S$ value of the bulk sulfur pool. Slow biogenic redox (red bar) fractionates significantly from bulk sulfur composition. Bidirectional arrows indicate that $\delta^{34}S$ values from precipitated pyrite will fall anywhere within the indicated zone for the duration of precipitation. In a closed system with limited sulfate availability (yellow field), rapid and slow reduction rates record initial low $\delta^{34}S$ values, but $\delta^{34}S$ values of pyrite increase as sulfate is progressively depleted from solution, creating a significant range in $\delta^{34}S$ values of ore zone pyrite. Unidirectional arrows indicate the progressive increase of $\delta^{34}S$ values as pyrite is precipitated. The precipitation of pyrite sequesters ^{32}S with continual ^{34}S enrichment in the remaining bulk sulfur pool and, consequently, latter phases of precipitated pyrite.

Rittenberg, 1964; Goldhaber and Kaplan, 1975; Habicht and Canfield, 1997; Seal, 2006; Gomes et al., 2017). In a system dominated by biogenic redox, biogenically generated pyrite should exhibit near-zero $\delta^{34}S$ values (assuming bulk sulfur $\delta^{34}S \approx 0‰$) with variability recording fluctuations in the bacterial activity and sulfate availability.

The sulfur isotopes of abiogenically derived pyrite will be influenced by Eh/pH changes. Oxidation of pyrite causes negligible fractionation (Nakai and Jensen, 1964; Rye et al., 1992; Ohmoto and Goldhaber, 1997; Brunner and Bernasconi, 2005; Seal, 2006), but the disproportionation of metastable sulfur species results in ^{34}S-enriched sulfate and ^{34}S-depleted H_2S (Agarwala et al., 1965; Granger and Warren, 1969; Habicht et al., 1998; Brunner and Bernasconi, 2005). This pattern of ^{34}S enrichment of sulfate and ^{34}S depletion of sulfides resulting from disproportionation will also occur through kinetic isotope fractionation under conditions of isotopic disequilibrium (Brunner and Bernasconi, 2005), substantiated by Granger and Warren (1969) through laboratory experimentation. Because the ^{34}S-enriched sulfate is nonreactive and removed with the groundwater, abiogenic ore zone pyrite precipitated in the process should always have lower $\delta^{34}S$ values than preexisting, diagenetic pyrite, and the $\delta^{34}S$ values recorded in each subsequent generation of ore zone pyrite should be lower than the predecessors (Brunner and Bernasconi, 2005). Further, in a system characterized by abiogenic pyrite recycling, the removal of kinetically inert sulfate will result in a continual decrease in available sulfides, decreasing the amount of abiogenic ore zone pyrite that will be derived with each subsequent generation. The extent of abiogenic fractionation is predominantly controlled by the rate of disproportionation reactions and will be at a maximum as reaction rates are slowed and kinetic isotope fractionation values approach equilibrium predictions (Ohmoto and Goldhaber, 1997; Seal, 2006). The primary influence on disproportionation kinetics is solution pH. In a synthesized roll front, Granger and Warren (1969) reported that intermediate sulfur species had longer residence time in more basic solutions. Disproportionation will fractionate more extensively as sulfur species equilibrate with increasing pH.

The degree of abiogenic sulfur fractionation is further dependent on Eh/pH conditions and aqueous sulfur speciation (Fig. 4). Fractionation will decrease with decreasing Eh across the roll front (Ohmoto, 1972) and increase with increasing pH (Sakai, 1968; Ohmoto, 1972). While this assumes a system at equilibrium and the extent of kinetic fractionation may be less than predicted values, the fractionation trends are not invalidated by precipitation under conditions of disequilibrium, and it is possible to identify Eh/pH gradients across the redox interface by sampling a transect of abiogenically derived pyrite spanning the roll front.

These predicted isotopic trends are summarized as follows:

Primary contrasts of biogenic and abiogenic redox:

1. Abiogenically derived pyrite will always have equal or lower $\delta^{34}S$ values compared to preexisting pyrite from which it is derived; biogenic pyrite may have $\delta^{34}S$ values higher than preexisting pyrite as the sulfur pool is depleted.
2. The quantity of pyrite will be continuously depleted in a system exhibiting abiogenic redox patterns, whereas a system reflecting biogenic redox may result in enrichment of pyrite within the ore zone compared to the quantity of sulfides preceding the orebody.

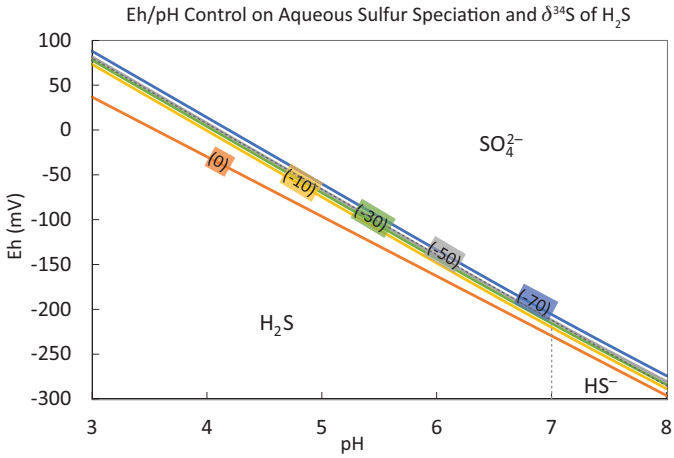

Fig. 4. The effect of Eh/pH conditions on aqueous sulfur speciation and subsequent $\delta^{34}S$ values of H_2S in solution. Dotted lines are the equilibrium boundary lines between aqueous sulfur species such as sulfate and H_2S. Intermediate sulfur species are not displayed because of eventual disproportionation. Colored lines track Eh/pH conditions that will produce a corresponding $\delta^{34}S$ value of H_2S (shown in parentheses in ‰). Temperature = 25°C; bulk sulfur $\delta^{34}S$ = 0‰. Energies of formation from Drever (1997); isotope equilibrium constants from Ohmoto and Goldhaber (1997).

Biogenically controlled redox:

1. Pyrite may be enriched in the ore zone compared to barren, unaltered core ahead of the roll.
2. $\delta^{34}S$ values of ore zone pyrite produced by prolific bacterial activity (rapid sulfate reduction) will show minimal fractionation from pre-ore pyrite $\delta^{34}S$ values.
3. $\delta^{34}S$ values of ore zone pyrite in an open system with unlimited sulfate availability will exhibit limited variation.
4. $\delta^{34}S$ values of ore zone pyrite in a closed, sulfate-limited system will show a broad range of fractionation values that will produce a fraction of pyrite heavier than initial pre-ore pyrite.

Abiogenically controlled redox:

1. Pyrite will be depleted in the ore zone compared to barren, unaltered sandstone, and the concentration of ore zone pyrite will progressively decrease toward the barren, altered core.
2. $\delta^{34}S$ values of ore zone abiogenic pyrite will be lower than those of pre-ore pyrite.
3. Abiogenic pyrite precipitated under low pH conditions will show limited fractionation from pre-ore pyrite values.
4. Abiogenic precipitation under neutral or basic pH will fractionate extensively from pre-ore pyrite.
5. Multiple generations of pyrite recycling will create progressively lighter ore zone pyrite.
6. $\delta^{34}S$ values will increase toward the barren, unaltered contact if there is an Eh drop across the roll.
7. $\delta^{34}S$ values will decrease toward the barren, unaltered contact if pH increases across the roll.

Deposit Characterization

Regional geology

The uranium roll-front deposits and associated rocks described in this contribution occur in Tertiary basins (Fig. 5) adjacent to uplifts of predominantly felsic Precambrian crystalline rocks. Both the Lost Creek and Willow Creek Mine Unit 10 deposits occur in host rocks of late Paleocene to early Eocene age: Lost Creek is hosted in the Battle Springs Formation, and Willow Creek Mine Unit 10 in the coeval Wasatch Formation (Sharp and Gibbons, 1964; Whipkey et al., 1991; Abzalov and Paulson, 2012). Both Battle Springs and Wasatch formations are comprised of extremely immature arkosic sands separated by layers of mudstone of variable thicknesses. Younger sedimentary rocks have been largely removed by erosion but consist of similar fluvial sandstones and mudstone, overlain locally by the intensely eroded and dissected volcaniclastic White River Formation (Sharp and Gibbons, 1964). Both formations host variable amounts of lignite layers and some large coal deposits, although, at most, only minor lignite occurs in the immediate vicinity of the deposits.

Host-rock and orebody petrography

All samples from both deposits are comprised of extremely immature, poorly sorted and poorly rounded, weakly indurated arkosic sediments with obvious provenance in the proximal Precambrian uplifts. Grains are angular to poorly rounded with sizes ranging from cobbles to fine sand in individual arkosic layers. Both authigenic clay forming after feldspar grains and clearly detrital clay (possibly after volcanic glass) are abundant; powder diffraction indicates mostly smectite with illite and minor kaolinite (Swapp, 2012). Detrital minerals consist of alkali feldspar, plagioclase, quartz, biotite, and chlorite with an extremely wide variety of accessory minerals including zircon, hornblende, garnet, epidote, sphene, monazite, iron-titanium oxides, pyrite, and rare barite. Pyrite is absent in the oxidized portions of the arkoses up the hydrologic gradient from the ore zone but exists as both framboidal aggregates and isolated pyrite grains within the ore zones at each site. Isolated grains vary in quality of their crystal habit from euhedral to anhedral (Figs. 6A, 7C, D, 8B; mineral abbreviations after Whitney and Evans, 2010) and are collectively referred to as subhedral to distinguish this morphological category from framboidal pyrite. Pre-ore, diagenetic pyrite is also present within the barren, unaltered sandstone ahead of both roll fronts.

The Lost Creek deposit occurs in the Great Divide Basin (Fig. 5); samples described in this report are from the M-Horizon, 425 to 450 ft in depth. The Great Divide Basin is distinctive in that it is hydrologically isolated from surrounding drainage systems (Heller et al., 2010). The hydrologic restriction of the basin has significant implications for the formation of local uranium orebodies, making it very probable that the Lost Creek deposit evolved as a geochemically closed system. In addition to the hydrological isolation, the Lost Creek deposit differs from the Willow Creek Mine Unit 10 deposit in the following critical respect: organic material is conspicuously rare in all samples examined. Pyrite framboids and subhedral crystals are present across the Lost Creek ore deposit and in the barren, unaltered rocks down hydrologic gradient from the roll front. Pyrite is most abundant within the barren, unaltered zone ahead of the roll and decreases systematically across the orebody toward the barren, altered zone (Fig. 9). Within the ore zone, pyrite is most abundant at the down-gradient nose of the deposit and never exceeds 0.17 wt % anywhere in the orebody. Pyrite subhedral crystals most commonly occur along cleavage planes in chlorite and biotite (Fig. 6A). Pyrite framboids occur in the clay matrix between the detrital grains (Fig. 6B). Uranium mineralization at Lost Creek occurs intermixed with both framboidal and

Fig. 5. Google Earth location map of the two study deposits: Lost Creek in the Great Divide Basin and Willow Creek Mine Unit 10 in the Powder River Basin.

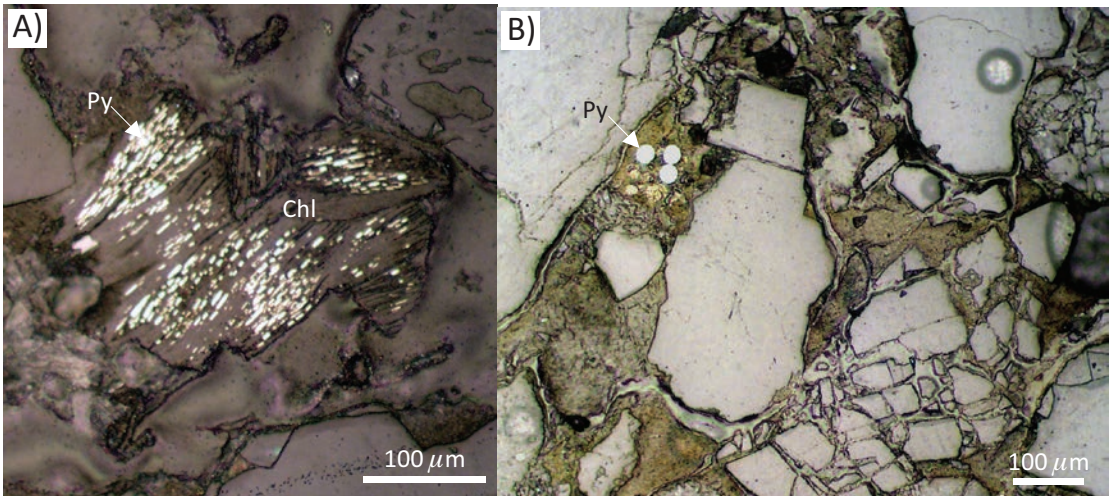

Fig. 6. Pyrite occurrences at Lost Creek. (A) is a reflected-light image in thin section of anhedral pyrite (Py) in chlorite (Chl). (B) is a reflected-light image in thin section of a framboid cluster formed in the host-rock clay matrix.

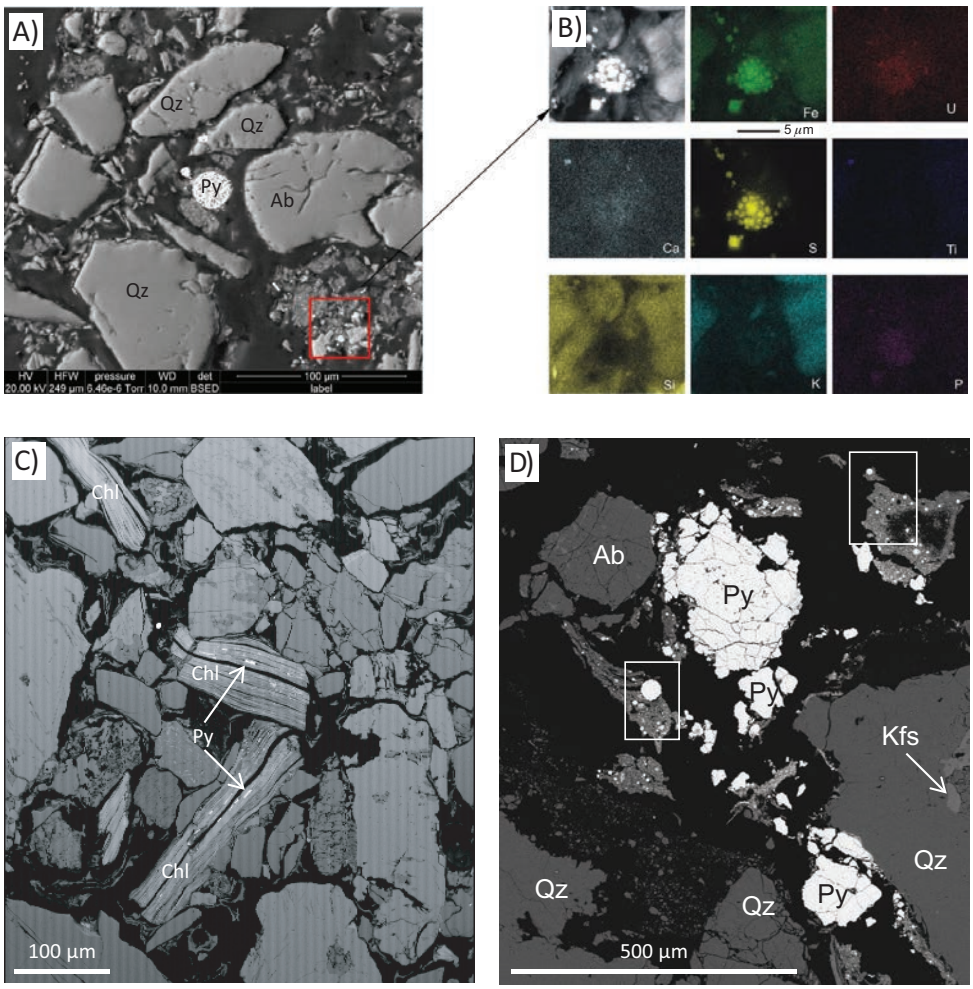

Fig. 7. Backscattered electron (BSE) images of uranium and pyrite mineralization at Lost Creek. (A) Coarse, angular detrital grains of quartz and feldspar with interstitial pyrite framboids; (B) enlargement of area in red box on A with pyrite framboid and associated weak uranium mineralization (uraninite); (C) anhedral pyrite forming along cleavages in chlorite (other detrital grains are quartz, albite, K-feldspar, epidote, and perthite); (D) areas in boxes include pyrite framboids and smectite with very fine grained, disseminated uranium mineralization appearing as bright specks (uraninite and/or coffinite). Several larger, anhedral pyrite crystals are labeled "Py"; they lack associated uranium mineralization in this image. The darkest areas between grains are epoxy. Mineral abbreviations: Ab = albite, Chl = chlorite, Kfs = K-feldspar, Py = pyrite, Qz = quartz.

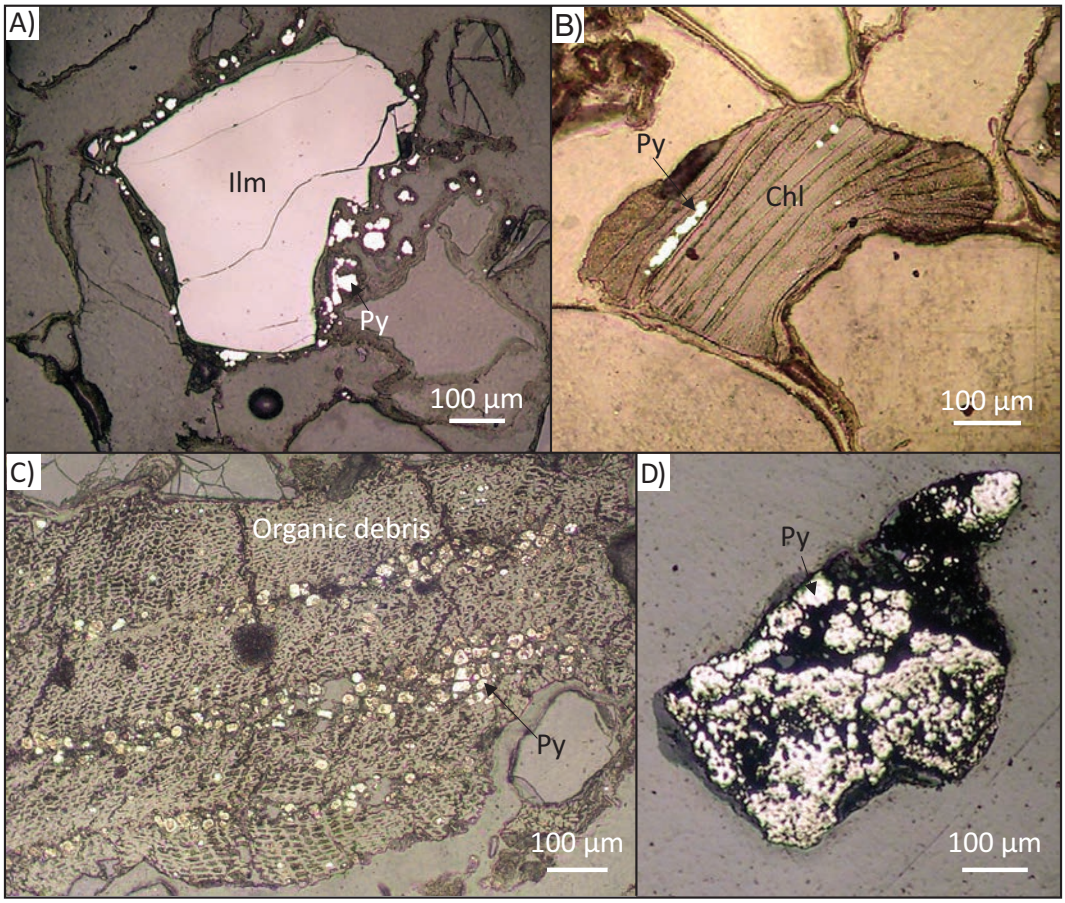

Fig. 8. Pyrite occurrences in Willow Creek Mine Unit 10. (A), (B), and (C) are reflected-light images in thin section, (A) of framboidal pyrite (Py) forming around ilmenite (Ilm), (B) of euhedral pyrite precipitated in chlorite (Chl), and (C) of framboidal pyrite in organic material. (D) is a reflected-light image of a pyrite grain mounted in an epoxy puck. The spheroidal texture clearly seen in the center of the grain indicates an agglomeration of framboids.

subhedral pyrite, as disseminated grains in intergranular clay (primarily Ca smectite), and in variable concentrations in rare organic material (Fig. 7). Coffinite, uraninite, brannerite, and

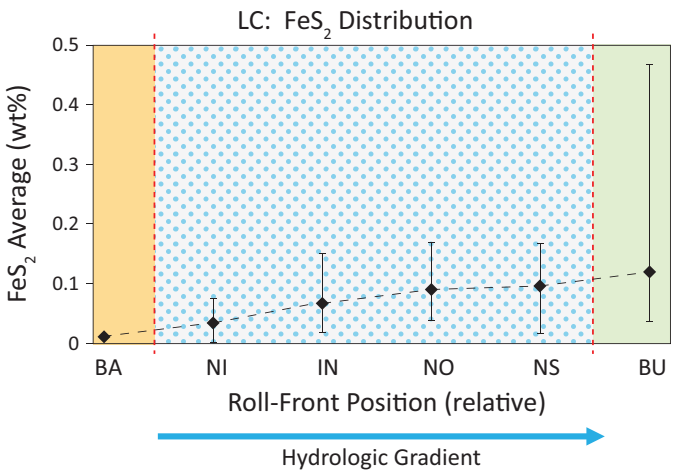

Fig. 9. Pyrite distribution across the roll front at Lost Creek (BA = barren altered, BU = barren unaltered, IN = interface, LC = Lost Creek, NI = near interior, NO = nose, NS = near seepage). Values displayed are averaged from a minimum of five samples per core. Error bars indicate maximum and minimum wt % measurements in each core.

one or more extremely fine grained uranium-bearing phases intergrown with clay have been recognized (Fig. 7D). Uranium occurs as a tetravalent ion in all identified phases; no phases containing hexavalent uranium or vanadates were recognized in the Lost Creek samples. Mineralization is sparse in all samples, and samples with high concentrations of uranium are extremely rare in this deposit. The observations that (1) both pyrite and uranium are absent in the oxidized portion of the arkosic rocks, (2) uranium mineralization is spatially associated with both subhedral and framboidal pyrite within the deposit, and (3) other obvious reductant phases are apparently absent in these samples all strongly indicate that pyrite mineralization was temporally associated with uranium mineralization in these samples.

The Willow Creek Mine Unit 10 deposit occurs on the westward-dipping flank of the eastern Powder River Basin (Fig. 5); samples described in this report are from Willow Creek Mine Unit 10, 350 to 400 ft in depth. In contrast to the Lost Creek deposit, these rocks are not hydrologically isolated; the aquifer is continuously recharged from the Black Hills region and discharges into the Powder River. Both pyrite (framboidal and subhedral) and organic material are abundant throughout Willow Creek Mine Unit 10 and, while pyrite is absent upgradient from the deposit, no systematic variation in pyrite

abundance was recognized across this deposit. Petrogenesis of pyrite at Willow Creek Mine Unit 10 strongly resembles its occurrence at Lost Creek. Pyrite subhedral crystals and amorphous grains occur intergrown with chlorite and biotite, within the host-rock matrix, and locally surrounding ilmenite grains (Fig. 8A, B). Pyrite framboids occur in the clay-rich matrix and associated with organic material (Fig. 8C, D). The abundance of pyrite at Willow Creek Mine Unit 10 has not been quantified because its distribution is extremely heterogeneous. Meaningful results would require a very large sample, and the significance of the resulting value to consideration of individual samples would be impossible to determine. Moreover, whole-rock analyses would not allow us to discriminate between sulfide sulfur and organically bound sulfur associated with the abundant and equally heterogeneously distributed organic material in these samples. Uranium mineralization at Willow Creek Mine Unit 10 typically occurs as coatings, as partial to complete replacements of detrital silicate grains, and associated with organic material (Fig. 10). Unlike Lost Creek, much of the uranium mineralization at Willow Creek Mine Unit 10 occurs as a hexavalent ion in vanadate (carnotite group) minerals. Uranium mineralization associated with pyrite is uncommon at Willow Creek Mine Unit 10, but carnotite group minerals form overgrowths on pyrite locally (Fig. 10D, E).

Although the amount of organic material has not been quantified through geochemical analyses, observations of core from hand sample and thin section in previous studies noted that substantial carbonaceous debris is present in the roll front at Willow Creek Mine Unit 10, whereas organic detritus at Lost Creek is minimal (Swapp, 2012; Nye, 2015). The relative abundance of organic material has been further corroborated with observations in thin section and hand sample in this study, which found that virtually no organic detritus remained within the roll front at Lost Creek. The only sizeable pieces of organic material at Lost Creek were identified in pre-ore core, unlike Willow Creek Mine Unit 10, in which large centimeter-sized detritus was identified throughout the roll front.

Ore mineral assemblages and postulated redox mechanisms

Preliminary observations suggested a correlation between pyrite occurrence, organic material, and redox mechanism. Although biogenically derived pyrite commonly forms from a

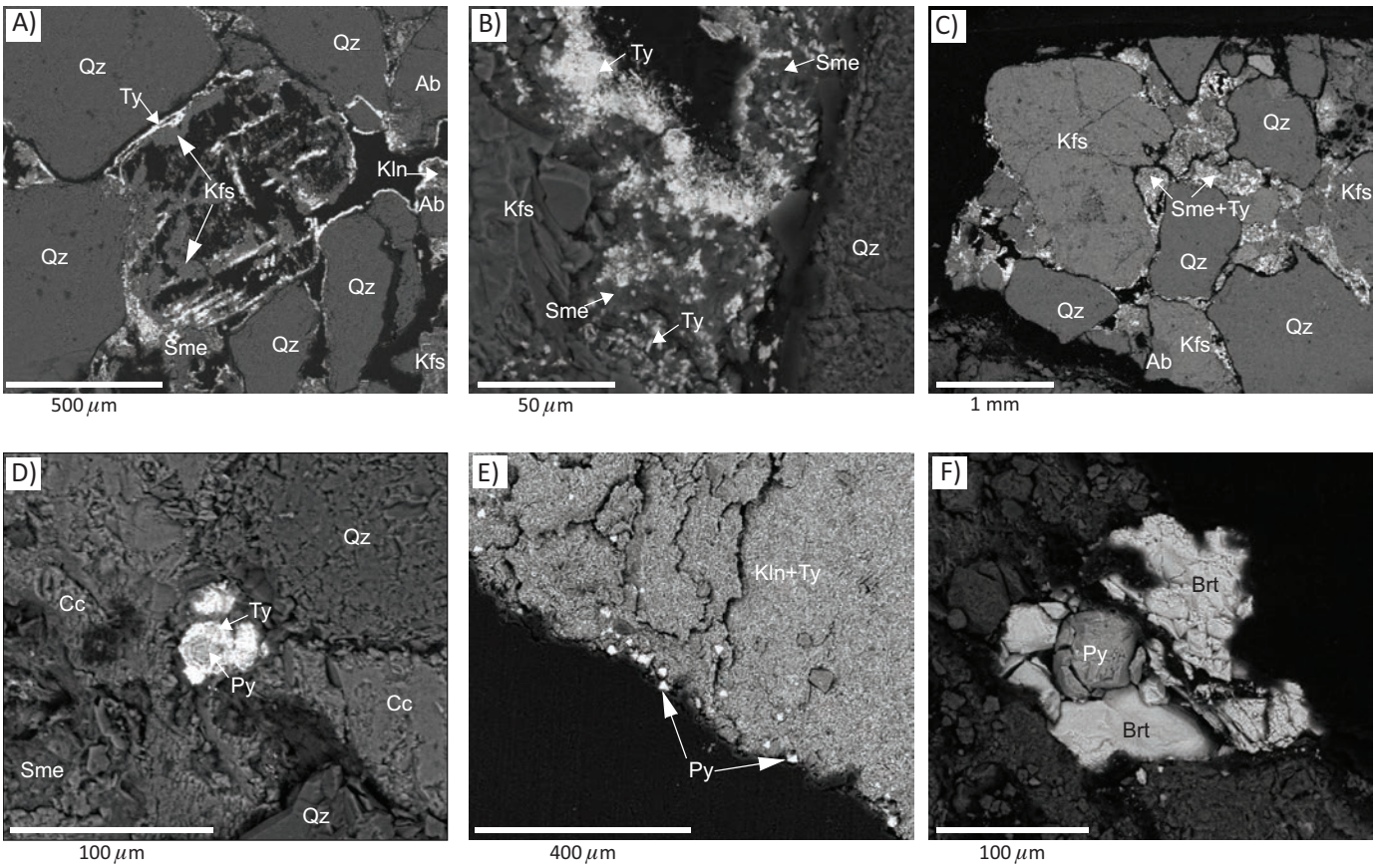

Fig. 10. Backscattered electron (BSE) images of uranium and pyrite mineralization at Willow Creek Mine Unit 10. Uranium mineralization (tyuyamunite) is only rarely spatially associated with pyrite. (A) Authigenic clay after K-feldspar with later tyuyamunite along edges and cleavages. (B, C) Interstitial clay (Ca smectite) and tyuyamunite between angular detrital grains in typical arkosic host rock. (D) Rare example of tyuyamunite overgrowth on pyrite associated with calcite, quartz, and smectite. (E) Pyrite octahedra in authigenic kaolinite with minor tyuyamunite after detrital feldspar. (F) Barite overgrowth on euhedral pyrite crystal with no associated uranium mineralization. The darkest areas not labeled with mineral abbreviations are epoxy. Mineral abbreviations: Ab = albite, Brt = barite, Cc = calcite, Kfs = K-feldspar, Kln = kaolinite, Py = pyrite, Qz = quartz, Sme = smectite, Ty = tyuyamunite.

precursor solid iron monosulfide phase such as mackinawite (Berner, 1970; Sawlowicz, 1993; Veeramani et al., 2013), which would significantly influence the reduction and immobilization of uranium in a roll-front system (Veeramani et al., 2013), no iron sulfide phases other than pyrite and marcasite (pyrite polymorph) were identified at either Lost Creek or Willow Creek Mine Unit 10. It is impossible to establish whether pyrite formed from an iron monosulfide precursor at these sites, and it is assumed that any iron monosulfide precipitated in the roll front has since been transformed to pyrite. Willow Creek Mine Unit 10 contains abundant organic material and abundant framboidal pyrite, and is dominated by tyuyamunite mineralization (Nye, 2015). Pyrite in the form of framboids is most commonly associated with organic material or occurs as large clusters in the interstitial matrix (Fig. 8C, D), whereas subhedral crystals are found in biotite and chlorite or rimming ilmenite grains (Fig. 8A, B). The abundant pyrite and the association with organic material suggest that Willow Creek Mine Unit 10 evolved through biogenic redox. Although no fluid inclusions in pyrite were found to verify the sulfur sources or S-isotope composition of the ore-forming fluid at Willow Creek Mine Unit 10, the greatest contribution of sulfur to the bulk sulfur pool most likely stemmed from pyrite recycling of pre-ore and ore zone pyrite. While organic material may have been the source of sulfur in pre-ore pyrite (and therefore its isotopic signature already incorporated into the bulk sulfur pool with analyses of pre-ore pyrite), the relative percentage of sulfur found in organic material of Wyoming Tertiary deposits is low (0.2–0.9%; Kehoe, 2018). It is expected that, due to its spatial association, framboidal pyrite incorporated a portion of organically bound sulfur; however, given the low sulfur percentages estimated in the organic material in these deposits, the contribution of organically bound sulfur to the bulk sulfur pool and overall isotopic signature of the ore-forming fluid was likely small. Similarly, minimal contribution of sulfate to the bulk sulfur pool is expected from influx of groundwater through overlying rock units. Nye (2015) noted an average of 65.7 ppm sulfate in groundwater from monitor wells surrounding Willow Creek Mine Unit 10 outside the mineralization zone, and other studies have identified that fresh water is typically characterized by extremely low concentrations of sulfate (Berner, 1984; Goldhaber, 2003).

Lost Creek contains scarce organic material and limited pyrite, which typically occurs as subhedral crystals or framboids in the clay matrix (Fig. 6B) or as subhedral grains in biotite and chlorite grains (Fig. 6A). The lack of organic material at Lost Creek is expected to limit bacterial activity, therefore suggesting roll-front propagation through abiogenic redox. Although there may be some disseminated organic material in the host-rock matrix at Lost Creek based on the spatial observations of framboidal pyrite, it is highly unlikely that enough organic material is present to be a consequential contributor of organically bound sulfur to the bulk sulfur pool. Similarly, sulfur sourced from groundwater migrating through overlying rock is likely also minimal (Berner, 1984; Goldhaber, 2003); therefore, pre-ore and ore zone pyrites are the most likely sources of sulfur in the bulk solution. The dominant uranium minerals at Lost Creek are coffinite, uraninite, and brannerite ($(U,Ca)(Ti,Fe)_2(O,OH)_6$; Johnson and Schmidt, 2007; Johnson, 2008; Swapp, 2012).

Methods

Sample selection

Because typical concentrations of sulfur in Tertiary coals of Wyoming are low (2.0% and 0.2–0.9%; Kehoe, 2018), it is assumed that pre-ore pyrite is the primary contributor of sulfur to the bulk sulfur pool and therefore can be used to establish the S-isotope composition of the ore-forming solutions at Lost Creek and Willow Creek Mine Unit 10. This study compares S-isotope compositions of pre-ore pyrite from barren, unaltered core located ahead of the roll with those of pyrite from across the orebody. At Willow Creek Mine Unit 10, redox contacts are visually evident. The ore zone core at Willow Creek Mine Unit 10 bisected a tail of the roll-front system, and a vertical transect sampling five depths across 8 ft was selected for analysis, spanning from the reduced, unaltered border to the altered sandstone contact (Fig. 11A). Core at Willow Creek Mine Unit 10 beyond the orebody in the barren, unaltered sandstone was sampled at two depths to obtain S-isotope measurements on pre-ore pyrite.

Redox contacts at Lost Creek were not easily identifiable, and gamma ray logs were used in addition to core photos to identify hot spots of uranium ore. Both vertical and horizontal

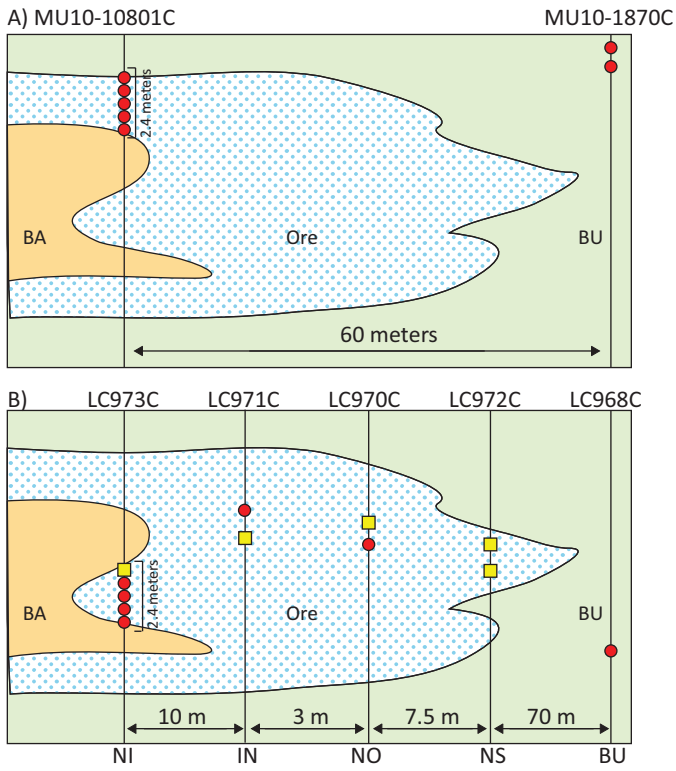

Fig. 11. Roll-front schematic showing sample locations for the vertical transect at Willow Creek Mine Unit 10 (MU10) (A) and the vertical and horizontal transects at Lost Creek (LC) (B). Red circles denote sample depths analyzing pyrite separates, and yellow squares both pyrite separates and thin sections. LC968C and MU10-1870C sample barren, unaltered core. LC973C was used for the vertical transect at Lost Creek and was also included with the other cores for the horizontal transect. Cores at Lost Creek are labeled with classification scheme for roll-front position. Within the ore zone, IN = interface, NI = near interior, NO = nose, NS = near seepage, ahead of the ore zone, BU = barren unaltered (no core depicted barren altered [BA] behind the ore zone). Not to scale.

transects were sampled at Lost Creek (Fig. 11B). The vertical transect was taken at the back of the roll from LC973C (near interior) for comparison with the tail sampled at Willow Creek Mine Unit 10 and to establish sulfur isotope behavior, with the initial Eh drop postulated to occur as the mineralizing solution passes into the roll (Granger and Warren, 1969; Rackley, 1972). The vertical transect sampled five depths spanning a total of 8 ft across a thin uranium lens bordered by altered sandstone at the top and base. The relative position within the roll front was determined based on proximity to altered sandstone contacts. The horizontal transect sampled four separate cores at approximately equivalent depths across the expanse of the roll-front system, approximately 70 ft. Core was also sampled ahead of the roll from LC968C barren, unaltered sandstone to establish pre-ore pyrite $\delta^{34}S$ values.

Sample preparation

In nearly all samples, pyrite constitutes less than 1% of the mineral constituents of the rock. We conducted a subset of secondary ion mass spectrometry (SIMS) analyses on polished thin sections to preserve isotopic values in their paragenetic context. However, in order to acquire a sufficiently large dataset for statistical significance in the interpretation of spatial isotopic trends, the majority of analyses were conducted on pyrite that was density separated from core samples. Pyrite morphologies and petrogenesis are consistent between the two mine localities, legitimizing data acquisition from density-separated grains within this study. Density-separated pyrite was mounted in EpoThin epoxy to make 1-in-diameter pucks. Pucks were polished with 1-μm diamond grit. Thin sections utilized for petrographic observations and in situ SIMS analyses were completed and polished by Vancouver Petrographics Ltd. from core samples that were impregnated with Pelco slow cure epoxy.

Mineral identification and element mapping

Basic petrographic studies were conducted on a Leica DM 2500P transmitted light microscope. Oxides, sulfides, and other opaque minerals were identified with a Nikon OPTIPHOT-POL microscope equipped with a reflected light source. Two instruments were utilized to confirm element composition of minerals in thin section and grains mounted in epoxy pucks: a JEOL JXA-8900R electron microprobe equipped with a Thermo NSS energy dispersive spectrometer, and an FEI Quanta FEG 450 field emission scanning electron microscope (FESEM) equipped with an Oxford Inca energy dispersive spectrometer and an Oxford HKL electron backscatter diffraction (EBSD) system. The microprobe was operated at 20 kV with a beam current of about 100 nA. All samples analyzed in the microprobe were carbon coated to reduce surface charging. Energy dispersive spectrometry (EDS) was utilized on the microprobe to identify all pyrite and nonpyrite grains mounted in epoxy pucks, confirm element composition of nonsulfide opaque minerals identified in thin section, and create element maps across pyrite grains in thin sections selected for SIMS analysis. Carbon coating was subsequently removed before SIMS analysis by polishing in colloidal silica suspension with a vibratory polisher.

Some pyrite grains mounted in epoxy pucks, especially from Willow Creek Mine Unit 10, were easily damaged through polishing. To avoid carbon coating and subsequent repolishing, some pucks were analyzed with the FESEM operated under low vacuum (0.23 Torr) with an accelerating voltage of 15 kV and spot size 3 for EDS element identification. Because pyrite and marcasite (low pH FeS_2 polymorph) have the same chemical composition, it was not possible to distinguish between the two minerals with EDS. EBSD on the FESEM was utilized to distinguish the FeS_2 phases of grains in pucks after SIMS analyses were completed. EBSD analyses were conducted under high vacuum (10^{-6}–10^{-7} Torr) with a stage tilt of 70°, spot size 5, and accelerating voltage of 20 kV. Samples studied with EBSD were ultrapolished for 1 h in a colloidal silica polishing suspension with a vibratory polisher. A thin carbon coat was applied to avoid charging.

Whole-rock geochemistry: Establishing pyrite wt %

Whole-rock geochemical analyses of Lost Creek samples were obtained in a separate study for UR-Energy by ALS Geochemistry. Total sulfur was measured using a Leco sulfur analyzer (ALS method code IR08). Organic material was volatized, and organic carbon and sulfur were removed during sample preparation (ALS Geochemistry, pers. commun., 2016). Because sulfate minerals are minimal or absent within ore zone samples, it was assumed that the total sulfur reported was generated from pyrite. Sulfur data were converted to pyrite wt % with the following equation:

$$S(wt\ \%) \times \frac{M_{FeS_2}}{M_S} = S(wt\ \%) \times \frac{119.97\ g\ FeS_2}{64.12\ g\ S_2} = FeS_2\ (wt\ \%).$$

No whole-rock geochemical data are available for Willow Creek Mine Unit 10.

Sulfur isotope analyses with SIMS

In situ sulfur isotope analyses were conducted with a Cameca 7f secondary ion mass spectrometer at the University of Manitoba, Winnipeg (Canada). Protocols similar to procedures documented by Ferrini et al. (2010) were used. All samples were gold coated to prevent surface charging. Sulfur isotope ratios ($^{34}S/^{32}S$) were measured using a ~1-nA Cs^+ primary beam accelerated at 10 kV with a spot size of ~15 μm filtered through a 247-μm entrance slit. The sample accelerating voltage was –8.7 kV with the electrostatic analyzer in the secondary column set to –9 kV, establishing a 300-V offset to reduce molecular interferences. Ions were detected with a Balzers SEV 1217 electron multiplier coupled with an ion-counting system. Overall dead time was 18 ns. $^{34}S^-$ and $^{32}S^-$ were measured sequentially by adjusting the magnetic field through 50 cycles and total analysis time of 7 min per point. Instrumental mass fractionation (IMF) induced during SIMS analysis was corrected with the Balmat pyrite standard (compositionally homogeneous, $\delta^{34}S$ = 15.1‰ Vienna-Canyon Diablo Troilite [V-CDT]) from the Balmat mine, New York (Sharpe, 2013). Some sample points for SIMS analyses were conducted on marcasite intergrown with pyrite. The Balmat pyrite standard was used for IMF correction for all FeS_2 polymorphs as crystal structure appears to have no or limited impact on IMF (Riciputi et al., 1998).

Two hundred fourteen analyses were obtained on pyrite from Willow Creek Mine Unit 10 and Lost Creek, most of them conducted on pyrite grains mounted in epoxy pucks.

A total of 78 points were analyzed for Willow Creek Mine Unit 10, 58 from ore zone samples and 20 from barren, unaltered sandstone. At Lost Creek, analyses were done on pyrite separates and in situ on grains in thin section. A total of 136 measurements were taken, 10 from barren, unaltered core and 126 from ore zone samples, 13 of which were conducted on thin sections. A variance equation (Sharpe and Fayek, 2016) was used to calculate 2σ errors reported with data, as follows:

$$2\sigma = \sqrt{1\sigma_{spot}^2 + 1\sigma_{session}^2 + 1\sigma_{Bal}^2},$$

where $1\sigma_{spot}$ is within spot error of each analysis point, $1\sigma_{session}$ is the spot-to-spot reproducibility (session error) from the standard deviation of measurements on the Balmat standard, and $1\sigma_{Bal}$ is the uncertainty of the Balmat standard (0.1‰).

Results

Lost Creek

Ore assemblages and FeS_2 characteristics: Pyrite at Lost Creek is scarce with no dominant morphology. The framboidal and subhedral morphologies are typically spatially isolated from one another. Both subhedral and framboidal pyrite can be found in the host-rock matrix (although rarely together), and subhedral pyrite also formed in biotite and chlorite. We suggest that the two morphologies are coeval within the deposit based on the following reasoning. First, there is no evidence that one pyrite morphology overprinted the other. Numerous studies that have identified multiple stages of pyrite formation have documented clear relationships of one morphology overprinting other preceding authigenic pyrite morphologies (Leibold, 2013; Ingham et al., 2014; Meek, 2014; Bonnetti et al., 2015). Moreover, during the recycling and redistribution process of pyrite, existing or altered surfaces of remnant pyrite have been identified as geochemically favorable nucleation sites for later stages of pyrite (Wilkin and Barnes, 1997; Kohn et al., 1998; Min et al., 2005). Due to the lack of evidence for overprinting or nucleation of a later pyrite morphology on preceding pyrite phases in the rare instances when both pyrite morphologies coexist (Fig. 7C), we infer that subhedral crystals and framboids formed contemporaneously through different redox mechanisms during ore formation.

No relic pre-ore pyrite grains were identified in the ore zone. The amount of pyrite progressively increases from barren, altered core (0.011 wt %) across the roll front with the greatest amount in the pre-ore core (0.121 wt %) ahead of the orebody (Fig. 9; UR-Energy, pers. commun., 2016). Given the reduction in quantity of pyrite by more than 10× from pre-ore core to altered core behind the roll, it is inferred that virtually all pre-ore pyrite was recycled during roll-front propagation. Marcasite was not identified within the deposit, and organic material at Lost Creek was also minimal. Zones of substantial calcite cementation were identified spanning the ore horizon and the barren, unaltered section.

Sulfur isotope values: Lost Creek sulfur isotope results displayed extreme variation. Sulfur isotope values ranged from –68.1 ± 0.4‰ to +142.8 ± 0.3‰ with a total difference of 210.9‰ (Fig. 12, App. 1). Pre-ore, diagenetic pyrite sampled from reduced, unaltered core collected ahead of the roll front was systematically ^{34}S enriched, producing values from –0.8 ± 0.5‰ to +70.6 ± 0.3‰. Subhedral pyrite within the ore zone varied from –68.1 ± 0.4‰ to +33.8 ± 0.3‰; framboidal pyrite ranged from –50.8 ± 0.5‰ to +142.8 ± 0.3‰. Pyrite was lightest within the vertical transect at Lost Creek that sampled the back of the roll at the altered contact (NI-LC973C, Fig. 12B). Framboidal pyrite in the vertical transect ranged from –50.8 ± 0.5‰ to +67.2 ± 0.4‰; subhedral pyrite ranged from –68.1 ± 0.4‰ to +19.2 ± 0.5‰. Within the vertical transect, subhedral pyrite showed an overall increase in $\delta^{34}S$ values progressing into the orebody (Fig. 12B). Data from the vertical transect have also been included in the horizontal transect (Fig. 12A). Framboidal pyrite within the horizontal transect ranged from –50.8 ± 0.5‰ to +142.8 ± 0.3‰. Subhedral pyrite ranged from –68.1 ± 0.4‰ to +33.8 ± 0.3‰. Subhedral pyrite $\delta^{34}S$ values in the horizontal transect exhibited an even more pronounced increase across the roll toward the unaltered contact (Fig. 12A). Most S-isotope analyses were performed on pyrite that was density separated. However, similar isotopic ranges and morphological distributions are exhibited from grains analyzed in thin section where petrographic relationships have been preserved (Fig. 13). Thin section analyses of framboidal pyrite produced a range of –41.2 ± 0.3‰ to +26.0 ± 0.3‰ with an average of –8.8 ± 0.3‰; thin section analyses of subhedral pyrite produced a range of –62.2 ± 0.3‰ to +33.8 ± 0.3‰ with an average of –27.5 ± 0.3‰. Subhedral pyrite in thin section analyses displayed the same trend of increasing $\delta^{34}S$ values across the roll toward the barren, unaltered contact.

Willow Creek Mine Unit 10

Ore assemblages and FeS_2 characteristics: Pyrite is abundant at Willow Creek Mine Unit 10; however, no whole-rock geochemical data are available to report an accurate wt %. The predominant pyrite morphology is framboidal (associated with organic material and in large clusters within the host-rock matrix; Fig. 8C, D) with a lesser frequency of subhedral pyrite precipitated in biotite and chlorite or rimming ilmenite grains (Fig. 8A, B). The two morphologies are spatially separated and appear coeval; as with the Lost Creek deposit, there is no evidence of overprinting or nucleation of a later pyrite morphology on preceding pyrite phases at Willow Creek Mine Unit 10. No relic grains of pre-ore pyrite were identified in ore zone samples for this study. Willow Creek Mine Unit 10 has considerable organic material with dark, organic-rich bands present throughout cored sections of the orebody.

Several additional paragenetic assemblages have been identified in Willow Creek Mine Unit 10 samples that were not present in the Lost Creek deposit. Marcasite was positively identified with EBSD (Fig. 14). Its occurrence was recognized exclusively within subhedral grains (never within framboids), and it was occasionally found as intergrowths with pyrite (Fig. 14), indicating coeval precipitation of both FeS_2 phases. Marcasite at Willow Creek Mine Unit 10 occurs near the altered sandstone contact within the ore zone, and its abundance decreases toward the reduced, unaltered border. Native selenium (Se^0), ferroselite ($FeSe_2$), and selenium-bearing pyrite ($Fe(S,Se)_2$; Fig. 15) have all

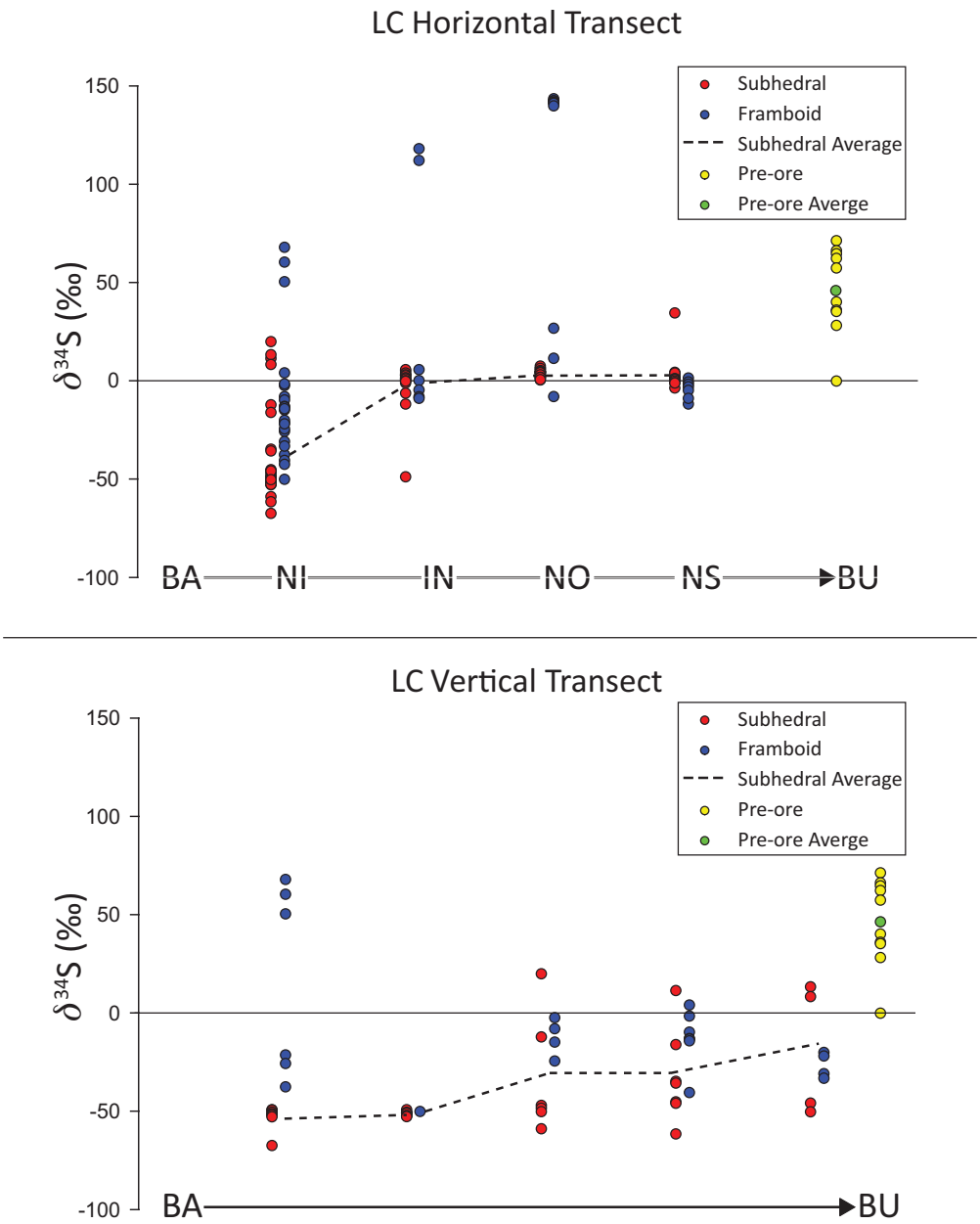

Fig. 12. $\delta^{34}S$ results from horizontal (A) and vertical (B) transects at Lost Creek (LC). Y-axis plots measured $\delta^{34}S$ values (error between 0.3 and 0.5‰), and x-axis plots relative position within the roll (BA = barren altered, BU = barren unaltered, IN = interface, NI = near interior, NO = nose, NS = near seepage). Blue data are framboids, red data subhedral crystals, and yellow data measurements on pre-ore pyrite. The green point corresponds to the pre-ore average. The dashed black line corresponds to the subhedral average across the ore zone.

been identified in core sampling the middle of the vertical transect at Willow Creek Mine Unit 10. Barite is also present within the deposit, occurring in some instances as a coprecipitate with ferroselite (Fig. 16). No areas of calcite cementation were identified in samples utilized in this study, eliminating carbonate as a possible pH buffer.

Sulfur isotope values: Sulfur isotope variation at Willow Creek Mine Unit 10 was considerably lower than at Lost Creek. Ore zone $\delta^{34}S$ values spanned from –45.1 ± 0.4‰ to +68.2 ± 0.4‰ with a total difference of 113.3‰. Pre-ore diagenetic pyrite also produced a considerable range, measuring from –48.1 ± 0.4‰ to +15.6 ± 0.5‰. Within the ore zone, framboidal pyrite varied from –32.5 ± 0.4‰ to +68.2 ± 0.4‰, and subhedral pyrite ranged from –45.1 ± 0.4‰ to +5.4 ± 0.4‰. Five sample points were conducted on marcasite within one sample depth at Willow Creek Mine Unit 10 (App. 2); marcasite displayed no variation in $\delta^{34}S$ values compared to subhedral pyrite at that depth. Subhedral pyrite exhibited increasing $\delta^{34}S$ values from the barren, altered contact across three sample depths; $\delta^{34}S$ values then markedly decreased again toward the reduced, unaltered border (Fig. 17, App. 2). No in situ S-isotope analyses were conducted on grains in thin section at Willow Creek Mine Unit 10.

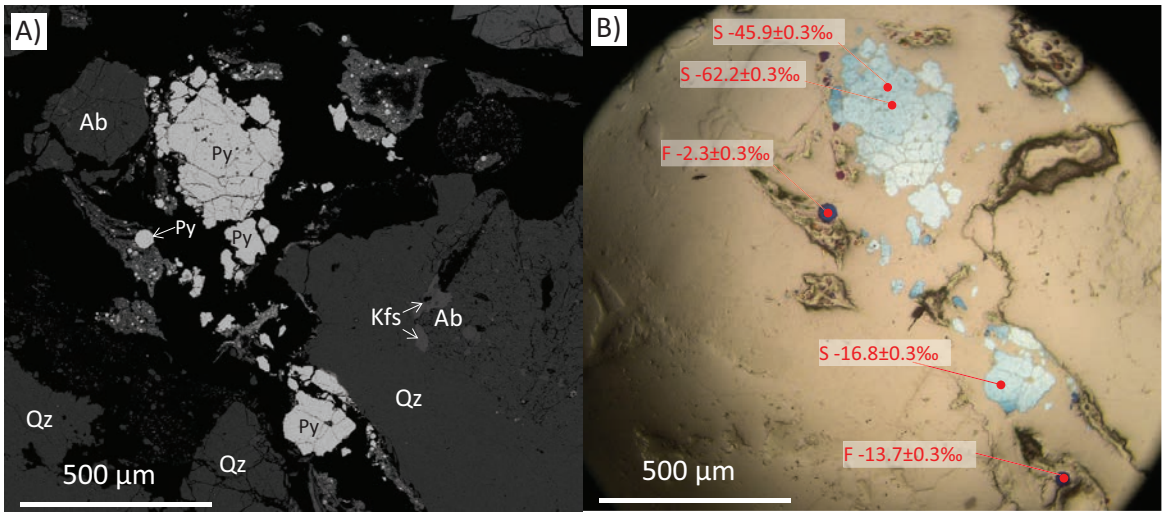

Fig. 13. Example of in situ sulfur isotope analyses conducted on a thin section from the near interior of the roll front at Lost Creek. (A) is a backscattered electron (BSE) image showing pyrite distribution within host-rock matrix in the vicinity of quartz and feldspar clasts. (B) is a reflected-light image in which locations and values of secondary ion mass spectrometry (SIMS) analyses are identified. The grain morphology is indicated with S (subhedral) and F (framboidal). Note that cool, iridescent colors are the result of very thin surface oxidation on pyrite grains. Oxidation is not expected to result in alteration of $\delta^{34}S$ values (Nakai and Jensen, 1964; Rye et al., 1992; Ohmoto and Goldhaber, 1997; Brunner and Bernasconi, 2005; Seal, 2006). Mineral abbreviations: Ab = albite, Kfs = K-feldspar, Py = pyrite, Qz = quartz.

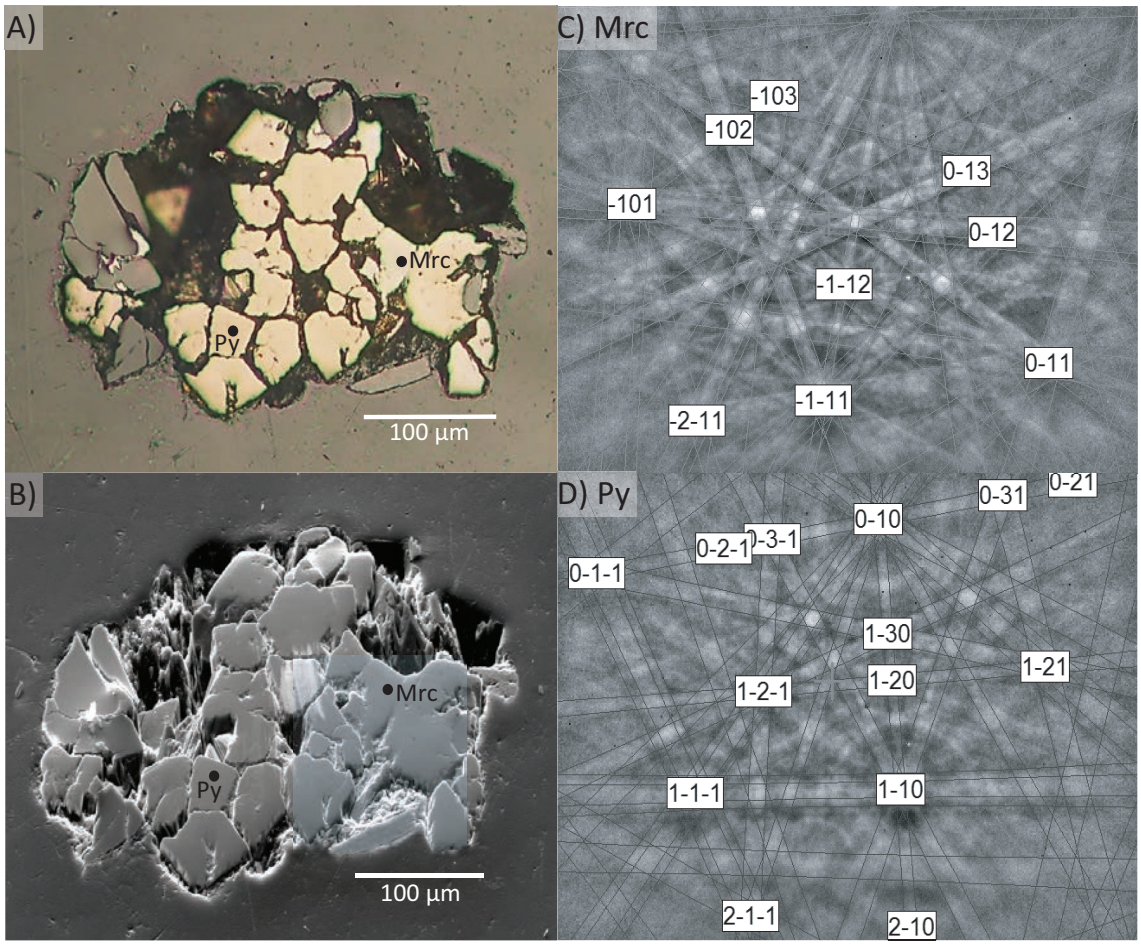

Fig. 14. Sulfide minerals in core near the altered contact at Willow Creek Mine Unit 10. (A) is a reflected-light image and (B) a secondary electron (SE) image identifying concurrent pyrite (Py) and marcasite (Mrc). (C) and (D) are electron backscatter diffraction (EBSD) Kikuchi line patterns of these grains of marcasite and pyrite, respectively.

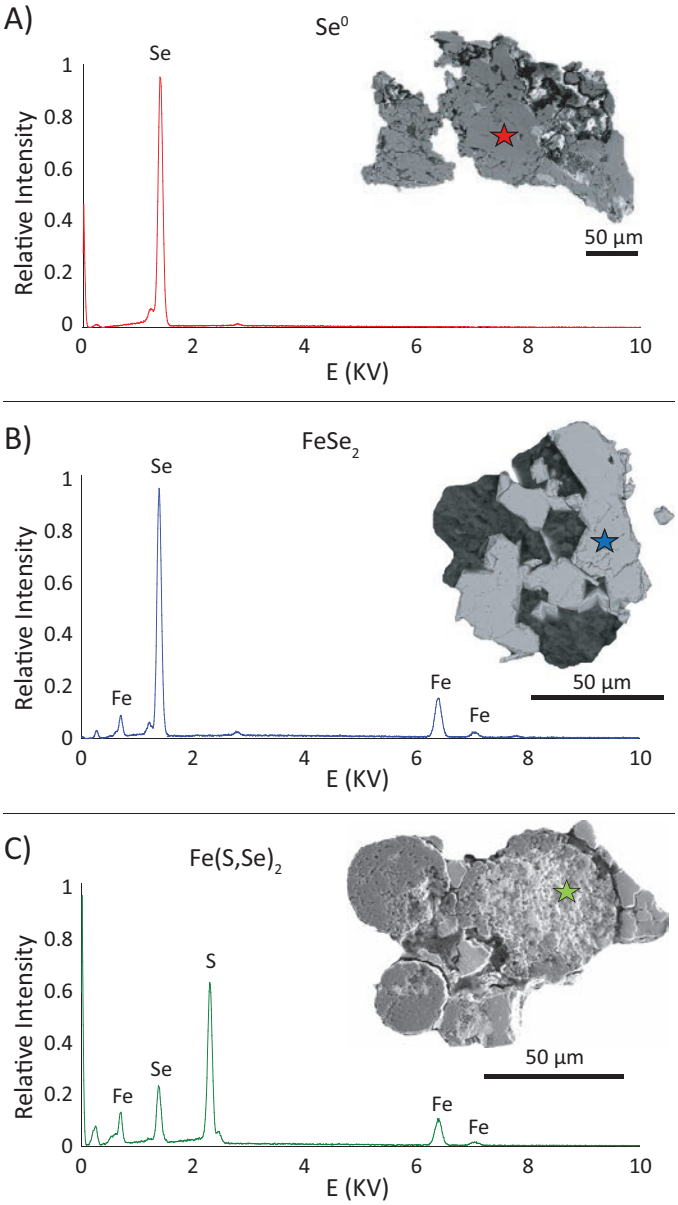

Fig. 15. Three selenium-bearing phases at MU10-10801C 384.5' identified with energy dispersive spectrometry (EDS) spectra on the microprobe. All spectra were measured on grains mounted in epoxy pucks. Backscattered electron (BSE) image indicating EDS analysis point is included with each plot. (A) is native selenium (Se^0), (B) is ferroselite ($FeSe_2$), and (C) is selenium-bearing pyrite ($Fe(S,Se)_2$) (note remnant gold coating from secondary-ion mass spectrometry [SIMS] analysis within framboid interstices makes portions of the grain appear lighter in BSE image). E = energy.

Discussion

Bimodal isotopic variation with pyrite morphology

A striking result of the sulfur isotope analyses is the differences in ranges of $\delta^{34}S$ values with pyrite morphology (Figs. 12, 17), with an overall average difference between pyrite morphologies greater than 22‰ at both sites. Comparing ore zone samples at Lost Creek, the average $\delta^{34}S$ value of subhedral pyrite was –16.7‰, while framboidal pyrite averaged +22.6‰. Willow Creek Mine Unit 10 ore zone subhedral pyrite averaged –26.6‰, and framboidal pyrite –4.5‰. At both Lost Creek and Willow Creek Mine Unit 10, subhedral pyrite produced the lowest $\delta^{34}S$ values, and subhedral pyrite never exhibited ^{34}S enrichment compared to pre-ore pyrite. On the other hand, framboidal pyrite at Lost Creek and Willow Creek Mine Unit 10 produced the highest $\delta^{34}S$ values with a fraction of grains that were heavier than pre-ore pyrite, exhibiting ^{34}S enrichment. A common approach to explain such isotopic variations is to attribute any low-value pyrite to biogenic redox and high-value pyrite to abiogenic redox, irrespective of pyrite morphology (Jensen, 1958; Cheney and Jensen, 1966; Leibold, 2013; Meek, 2014; Bonnetti et al., 2015). We have already established that abiogenic pyrite recycling will generate ^{34}S-depleted pyrite and produce sequentially lighter pyrite with each recycling event (Agarwala et al., 1965; Granger and Warren, 1969; Goldhaber et al., 1978), invalidating this assumption.

Another interpretation commonly invoked to explain bimodal isotopic variation is multiple independent fluid events from different sulfur sources with different bulk sulfur isotope compositions (Ingham et al., 2014). This concept is inapplicable to Lost Creek and Willow Creek Mine Unit 10, where temporal evidence suggests that framboidal and subhedral pyrite formed coevally. Moreover, it seems highly improbable that the same two fluid events created such similar patterns of $\delta^{34}S$ values with pyrite morphology at Willow Creek Mine Unit 10 and Lost Creek, as the two deposits are separated by hundreds of miles, and the Great Divide Basin, host to Lost Creek, is hydrologically isolated from the Powder River Basin, where Willow Creek Mine Unit 10 precipitated.

A third explanation exists, however, if pyrite morphology correlates to its biogenic or abiogenic mode of formation. Bonnetti et al. (2017) recently published a study in which they recognize the correlation between pyrite morphology and $\delta^{34}S$ values: in situ SIMS analysis of framboidal pyrite from the Baxingtu uranium deposit, northeast China, documented a range of $\delta^{34}S$ values from –72.0 to –14.4‰, whereas subhedral pyrite varied from –5.7 to +24.8‰. They attributed the sulfur isotope compositions of the framboidal and subhedral pyrite to biogenic and abiogenic processes, respectively. This approach is not only a satisfactory explanation for the observed bimodal isotopic variation at Lost Creek and Willow Creek Mine Unit 10, but it also offers an explanation for the contemporaneous formation of framboidal and subhedral pyrite, which cannot be derived from the same solution under the same chemical conditions by the same precipitation mechanism because of the differences in their free energies of formation. It is unlikely that the S-isotope signature of the ore-forming solution varies greatly within the bulk system on the microscale, suggesting that precipitation mechanism is the driver for morphological and isotopic differences. Given the exclusive spatial occurrences of both morphologies, it is logical to infer the biogenic origin of framboids in conjunction with organic material, and likewise the abiogenic formation of subhedral crystals on phyllosilicate substrates due to their inherent interface reactivity. The combined appearance of framboids and subhedral crystals in the host-rock matrix at Lost Creek and Willow Creek Mine Unit 10 can be explained by the presence of both disseminated clays and disseminated organics in the interstices.

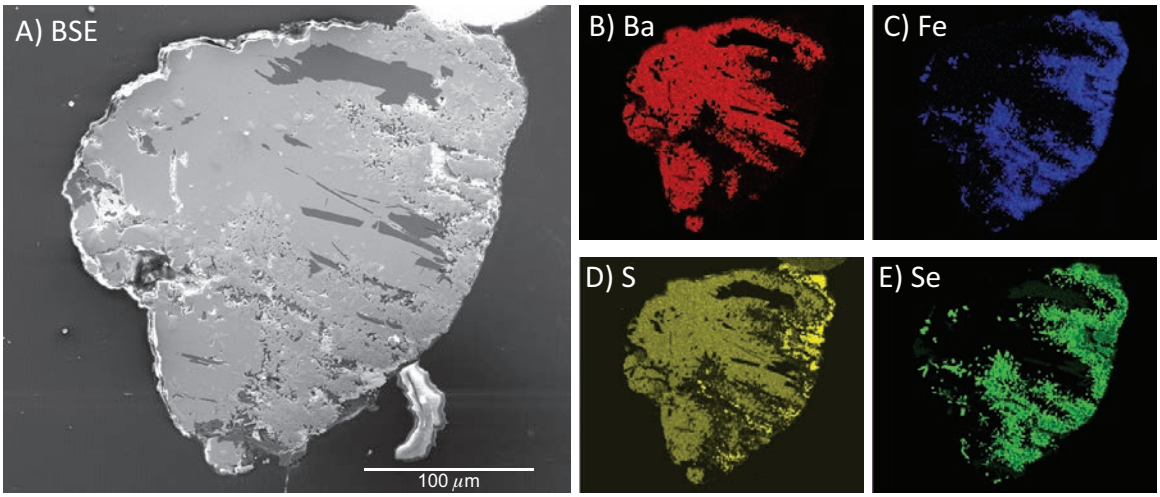

Fig. 16. Backscattered electron (BSE) image (A) showing coprecipitated barite and ferroselite in a grain separate from MU10-10801C 384.5'. Selenium-bearing pyrite is also present along the right-hand perimeter of the grain, which precipitated prior to ferroselite and barite. The BSE image is accompanied with element maps of barium (B, red), iron (C, blue), sulfur (D, yellow), and selenium (E, green).

Additionally, a number of studies have indicated that framboidal pyrite has a biogenic origin. While there has been successful abiotic laboratory precipitation of framboidal pyrite, synthesized framboids, especially at low temperatures, are not easily preserved under sterile conditions (Farrand, 1970; Kribek, 1975; Sawlowicz, 1993). Farrand (1970) documented that synthetic framboids rapidly developed into homogeneous subhedral crystals if left in solution, and Kribek (1975) noted that framboids were significantly more durable in the presence of humic substances. More recent high-resolution electron imaging of framboids within a preserved biofilm has proven that an organic matrix surrounding individual grains provided a critical form for the framboidal framework (MacLean et al., 2008). The role of bacteria in the generation of framboids has historically been debated because microbial biofilms are not readily preserved and had not previously been observed in direct correlation with framboidal pyrite. The work of MacLean et al. (2008) directly addresses this main point of controversy and substantiates the proposed biogenic origin of framboids, which correlates with the ranges of framboidal $\delta^{34}S$ values identified at Lost Creek and Willow Creek Mine Unit 10.

At both deposits, a fraction of framboidal pyrite exhibited ^{34}S enrichment compared to pre-ore pyrite, as predicted by sulfate depletion through biogenic redox and contradictory to ^{34}S removal anticipated by abiogenic redox. In contrast, the subhedral $\delta^{34}S$ values corroborate isotopic fractionation patterns proposed for abiogenic redox: subhedral pyrite consistently produced the lowest $\delta^{34}S$ values within the ore zone at Lost Creek and Willow Creek Mine Unit 10 and never

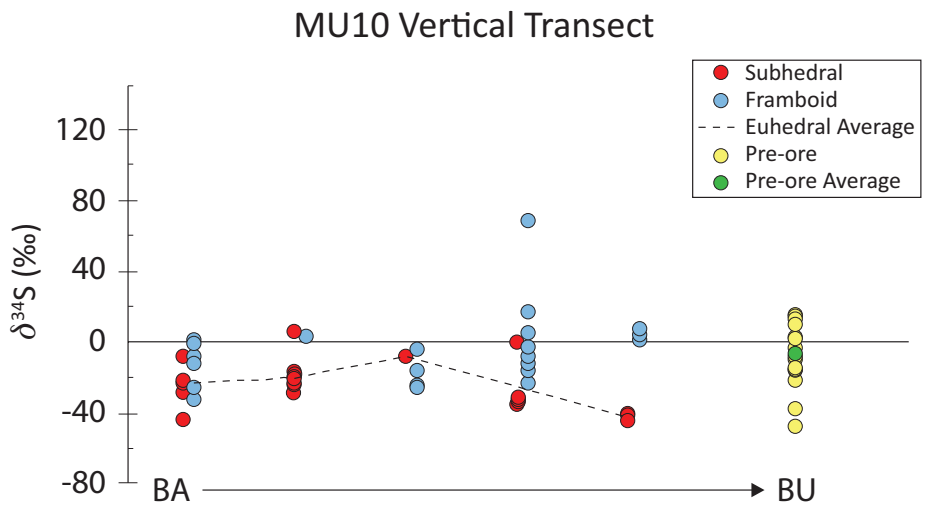

Fig. 17. $\delta^{34}S$ results from vertical transect at Willow Creek Mine Unit 10 (MU10). Y-axis plots measured $\delta^{34}S$ values (error between 0.3 and 0.5‰), and x-axis plots relative position within the roll (BA = barren altered, BU = barren unaltered). Blue data are framboids, red data subhedral crystals, and yellow data measurements on pre-ore pyrite. The green point corresponds to the pre-ore average. The dashed black line corresponds to the subhedral average across the ore zone.

generated $\delta^{34}S$ values higher than pre-ore pyrite. This suggests an abiotic origin for subhedral pyrite and indicates that both biogenic and abiogenic redox contributed to ore formation within these deposits. Dissecting the results using pyrite morphology to distinguish redox mechanism allows us to constrain both prolificacy of bacteria and chemical conditions of formation at each deposit.

Lost Creek

Biogenic influence: The isotopic variation in biogenically derived pyrite at Lost Creek is unprecedented, reflecting extreme Rayleigh fractionation. Framboidal $\delta^{34}S$ values at Lost Creek ranged from –50.8 ± 0.5‰ to +142.8 ± 0.3‰, recording a difference of 193.6‰ (Fig. 12). Because of the hydrologic isolation of the Great Divide Basin (Heller et al., 2010), the Lost Creek deposit is believed to have evolved as a closed system. Rayleigh fractionation manifests from closed-system behavior (Ohmoto and Goldhaber, 1997; Seal et al., 2000; Seal, 2006), in this case resulting from the limitation of sulfate within the Lost Creek deposit. As pyrite is precipitated, the remaining sulfate and, consequently, the progression of pyrite become increasingly ^{34}S enriched as ^{32}S is continuously removed from solution. With enough sulfur sequestration, this will produce a fraction of grains that are much heavier than the initial sulfate pool (Ohmoto and Goldhaber, 1997; Seal et al., 2000; Seal, 2006). Given the lack of organic material and other sulfur-bearing minerals at Lost Creek, the most feasible sulfur source for the ore-forming solution is the pre-ore diagenetic pyrite, which is already isotopically ^{34}S enriched, ranging from –0.8 ± 0.5‰ to +70.6 ± 0.3‰ (Fig. 12). Of the 47 framboids measured within the ore zone, only 10 were heavier than pre-ore pyrite, and most were significantly lighter. Using the average $\delta^{34}S$ value of pre-ore pyrite (45.4‰) to define the $\delta^{34}S$ value of the bulk sulfur pool, the framboid data were modeled with a Rayleigh fractionation curve (Fig. 18; App. 3). The highest $\delta^{34}S$ value (142.8 ± 0.3‰) measured in framboidal pyrite corresponds to approximately 90% depletion of sulfate in the system. The bulk sulfur pool summed from the $\delta^{34}S$ values of ore zone framboidal pyrite and remnant sulfate at 90% depletion equates to 46.8‰, producing an error of 3.03% in the Rayleigh model.

In addition to limited sulfate availability resulting in extremely ^{34}S enriched pyrite, the extent of isotopic variation at Lost Creek would also have required substantial fractionation from the initial bulk sulfate pool to produce framboidal pyrite as light as –50.8‰. The lightest ore zone framboid is 50‰ lighter than the lightest pre-ore pyrite. This implies a slow rate of bacterial reduction within the Lost Creek deposit (Harrison and Thode, 1958; Kaplan and Rittenberg, 1964; Goldhaber and Kaplan, 1975; Habicht and Canfield, 1997; Seal, 2006) and indicates restricted bacterial activity. This is consistent with the observed paucity of organic material that would inhibit the establishment of a prolific SRB system and is further substantiated by the pyrite distribution trend across Lost Creek (Fig. 9). Instead of an enrichment of pyrite within the ore zone, which would be expected from additional H_2S generation through substantial biogenic redox, the maximum amount of pyrite at Lost Creek is within barren, unaltered core beyond the roll front. Within the orebody, the amount of pyrite is greatest at the barren, unaltered border and consistently decreases toward the barren, altered contact. The pyrite distribution follows the depletion pattern expected from the abiogenic pyrite recycling process. Oxidation from the solution front would predominantly strip pyrite at the altered

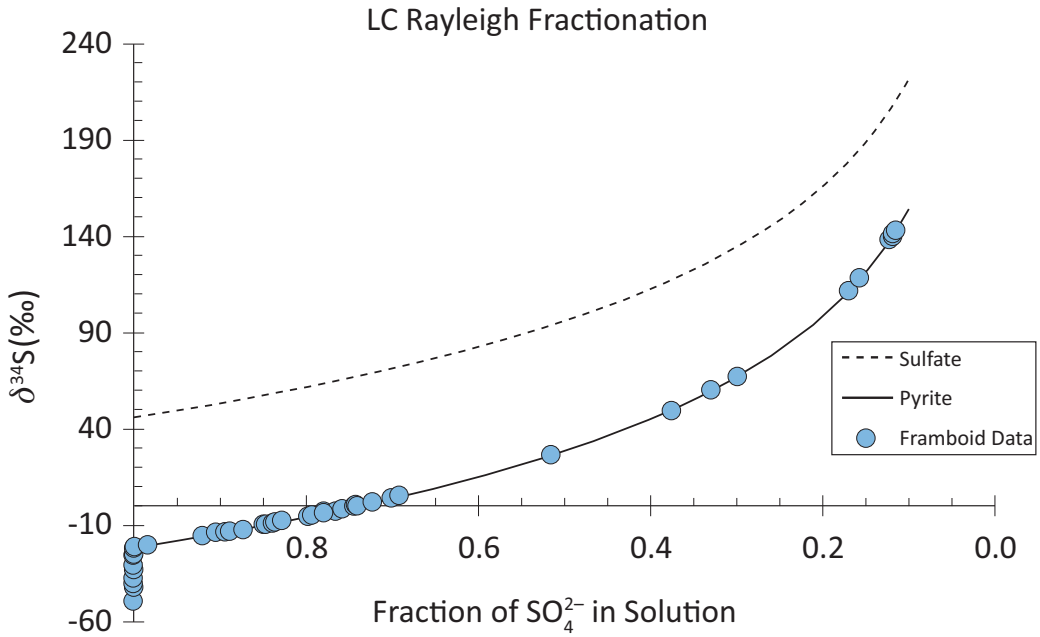

Fig. 18. Rayleigh fractionation model of framboidal pyrite at Lost Creek (LC). The dashed line models $\delta^{34}S$ value of sulfate in solution with progressive sulfur depletion. The solid black line is the $\delta^{34}S$ value of pyrite produced at a specific level of depletion. The blue circles are framboid data. The bulk $\delta^{34}S$ value of the solution and the initial $\delta^{34}S$ value of sulfate for the Rayleigh model were taken as the average $\delta^{34}S$ value of pre-ore pyrite, 45.4‰. The model assumes maximum fractionation at 25°C ($\Delta^{34}S_{FeS_2\text{-}SO_4^{2-}} \approx$ –67.75‰). Data exhibiting fractionation in excess of –67.75‰ from the pre-ore pyrite average were normalized to for fraction of SO_4^{2-} in solution. Data correspond to 88.5% depletion of solution sulfate.

contact with decreasing effect as the solution progresses through the roll. This indicates abiogenic pyrite recycling as a greater influence over system redox than SRB. Although biogenic redox occurred at Lost Creek, the distribution of pyrite and isotopic evidence from framboids indicate that it and its potential chemical influences on the ore-forming solution were limited.

Abiogenic sulfur isotope trends: The indications from bacterially derived pyrite at Lost Creek suggest that the deposit was only nominally influenced by biogenic redox processes, and the isotopic trends from abiogenically derived pyrite identify ore formation under more neutral conditions than those established in a prolific bacterial system. Even with the extreme fractionation recorded in biogenically derived pyrite at Lost Creek, the lightest pyrites analyzed were subhedral, producing values as low as –68.1 ± 0.4‰ (Fig. 12, App. 1). The abiogenically derived pyrite at Lost Creek was, on average, over 62‰ lighter than pre-ore pyrite. The extent of abiotic fractionation is far greater than reported from experimental disproportionation measurements (maximum $\Delta^{34}S_{sulfate\text{-}H_2S}$ = 23‰ from Granger and Warren, 1969), indicating multiple generations of pyrite recycling. The spatial distribution of $\delta^{34}S$ values showed a gradual increase in ^{34}S incorporation across the roll from the altered, oxidized contact to the reduced, barren border. The trend is seen most clearly in the horizontal transect that spans the entire deposit (Fig. 12A) and is mimicked on a smaller scale in the vertical transect sampling the back of the roll at Lost Creek (Fig. 12B). The gradual increase in $\delta^{34}S$ values across the Lost Creek deposit corresponds to an Eh drop as the solution front passed through the ore zone. The greatest effect of Eh on the extent of sulfur isotope fractionation occurs across a ~50-mV window (Fig. 4). Because of the dependence of fractionation on sulfur speciation and the increased stability and activity of H_2S or HS^- in solution under more reducing conditions, abiogenic fractionation of S isotopes will be roughly constant for Eh conditions below this zone (Ohmoto, 1972). This trend is apparent along the horizontal transect, which uncovered the greatest isotopic variation along the altered contact from –68.1 ± 0.4‰ to +19.2 ± 0.5‰. The three cores sampling the interior and front of the roll showed higher, more consistent $\delta^{34}S$ values (Fig. 12A), indicating that the Eh drop persisted across the roll.

There is no evidence for a pH gradient at Lost Creek, however. On the contrary, the extent of fractionation at the altered sandstone border of Lost Creek suggests that the mineralizing solution was near neutral as it flushed into the deposit. Kinetic fractionation will approach equilibrium fractionation as reaction rates are slowed (Ohmoto and Goldhaber, 1997; Seal, 2006). The rates of disproportionation reactions are the largest control on the extent of abiogenic fractionation and are depressed with increasing pH (Granger and Warren, 1969). The first generation of recycled pyrite in the near seepage zone at the front of the roll averaged 2.6‰, already 42.8‰ lighter than the average pre-ore pyrite (Fig. 12A). This expresses significantly greater fractionation from disproportionation reactions than established experimentally (Agarwala et al., 1965; Granger and Warren, 1969), implying longer residence time of intermediate sulfur species in a neutral or basic pH solution. Subhedral pyrite from the vertical transect averaged –41.1‰, 86.5‰ lighter than average pre-ore pyrite (Fig. 12B), showing similarly extensive fractionation behavior in subsequent pyrite generations at the back of the roll, which indicates that the mineralizing solution was not strongly acidified in advance of the orebody.

Chemical conditions constrained by ore zone mineralogy: Given the scarcity of pyrite in the Lost Creek deposit, the impact of sulfide oxidation on solution pH would be limited and appreciable acidification unlikely. Moreover, the absence of marcasite (low pH polymorph of pyrite) at Lost Creek suggests ore precipitation at a pH above 5 (Murowchick and Barnes, 1986), and the pockets of calcite cementation throughout the deposit indicate a buffered, basic ore-forming solution front. Although SRB were present in the Lost Creek deposit, abiogenic sulfur isotope trends intimate that typical Eh/pH gradients generated by prolific biogenic redox were not established across the roll. Instead, biogenically derived pyrite indicates restricted bacterial activity, and abiogenically derived pyrite confirms that ore formation was predominantly driven by an Eh drop with a limited pH gradient across the redox interface. The Lost Creek deposit advanced through abiogenic pyrite recycling in a buffered solution at near-neutral pH.

Willow Creek Mine Unit 10

Biogenic influence: Willow Creek Mine Unit 10 framboidal $\delta^{34}S$ values ranged from –32.5 ± 0.4‰ to +68.2 ± 0.4‰, producing a total difference of 100.7‰ (Fig. 17). While this presents considerable isotopic variation comparable to that of the Lost Creek deposit, only one ore zone framboid showed ^{34}S enrichment relative to pre-ore pyrite. Excluding the ^{34}S-enriched outlier, framboidal pyrite at Willow Creek Mine Unit 10 ranged from –32.5 ± 0.4‰ to +17.2 ± 0.5‰, exhibiting the same range in isotopic signatures as pre-ore pyrite, which ranged from –48.1 ± 0.4‰ to +15.6 ± 0.5‰. The minimal fractionation of ore zone framboids from pre-ore pyrite implies rapid bacterial sulfate reduction (Fig. 3; Harrison and Thode, 1958; Kaplan and Rittenberg, 1964; Goldhaber and Kaplan, 1975; Habicht and Canfield, 1997; Seal, 2006), and the anomalously ^{34}S enriched pyrite is most likely the result of a locally isolated, sulfur-limited pocket in a solution otherwise exhibiting open-system behavior. Previous observations of Willow Creek Mine Unit 10 core noted the prominence of framboidal pyrite, which indicates significant biogenic influence, and an abundance of organic material available for sustained SRB activity. Given these observations in conjunction with the isotopic evidence, biogenic redox appears to have been critical in the establishment of the Willow Creek Mine Unit 10 roll-front system.

Abiogenic sulfur isotope trends: The chemical influences that the prevalent bacterial activity imposed on the ore-forming solution at Willow Creek Mine Unit 10 are recorded in the sulfur isotope trends from abiogenically derived ore zone pyrite. Subhedral pyrite produced the lowest $\delta^{34}S$ values in the ore zone at –45.1 ± 0.4‰, which are, on average, 20‰ lighter than those of pre-ore pyrite. Abiogenic fractionation at Willow Creek Mine Unit 10 was minimal compared to Lost Creek, and, unlike Lost Creek, the isotopic composition recorded at the redox boundary at Willow Creek Mine Unit 10 indicates an acidic solution front. The average $\delta^{34}S$ value from subhedral

pyrite sampled at the altered contact of Willow Creek Mine Unit 10 (Fig. 17) is –23.8‰, only 17.2‰ lighter than average pre-ore pyrite (–6.6‰). The extent of abiogenic fractionation is less than experimental values, indicating rapid disproportionation reactions driven at low pH (Granger and Warren, 1969). The data defined a clear trend in the spatial distribution of $\delta^{34}S$ values from subhedral pyrite across the deposit (Fig. 17). The $\delta^{34}S$ values initially increase away from the altered sandstone contact into the ore zone and then markedly decrease again toward the reduced, unaltered sandstone border. In the postulated biogenic redox model, the mineralizing solution is acidified in advance of the orebody, and it undergoes an Eh drop as it passes into the roll (Rackley, 1972). This Eh drop correlates to a decrease in sulfur isotope fractionation, producing the observed increase in $\delta^{34}S$ values (Fig. 4; Ohmoto, 1972). The subsequent decrease in $\delta^{34}S$ values will occur as pH is buffered across the roll, causing an increase in fractionation with deacidification (Fig. 4; Sakai, 1968; Ohmoto, 1972). This pattern follows the expected Eh/pH gradients generated in a biogenically established system, which is characterized by an Eh drop and initially acidic conditions that are neutralized as the solution front approaches the reduced, barren zone with prolific SRB activity (Jones and Starkey, 1962; Kuznetsov et al., 1963; Rackley, 1972). The isotopic evidence from abiogenically derived pyrite confirms chemical conditions across the Willow Creek Mine Unit 10 roll front indicative of a system dominated by biogenic redox and in agreement with isotopic signatures from framboidal pyrite.

Chemical conditions constrained by ore zone mineralogy: The presence of selenium at Willow Creek Mine Unit 10 supports the isotopic interpretation of an Eh drop across the roll. Selenium is a trace element that commonly enriches roll-front deposits, and its geochemical behaviors mimic those of sulfur (Howard, 1977). Three selenium-bearing phases have been identified in core sampling the middle of the vertical transect: native selenium (Se^0), ferroselite ($FeSe_2$), and selenium-bearing pyrite ($Fe(S,Se)_2$; Fig. 15). The co-occurrence of native selenium and ferroselite marks a redox boundary between Se^0 and Se^{1-} at an Eh just below 0 V (Fig. 19). The redox bounds of pyrite extend below the stability field of ferroselite in a mixed Fe-S-Se solution, and the partial substitution of selenium in pyrite will occur under more reducing conditions (Howard, 1977). The selenium-bearing phases within this one sample depth at Willow Creek Mine Unit 10 establish the Eh gradient observed in FeS_2 isotope signatures.

Further mineralogical evidence also bolsters the isotopic pH interpretations at Willow Creek Mine Unit 10. To simplify sulfur isotope analyses, iron disulfides herein have been collectively termed "pyrite," a nomenclature that encompasses marcasite. While this is acceptable for S-isotope comparison between morphologies, differentiating the specific iron disulfide polymorph becomes important when considering pH conditions. Experimental evidence has shown that marcasite will begin to precipitate with pyrite below pH 5 and increase in proportion to pyrite with decreasing pH (Murowchick and Barnes, 1986). Marcasite has been identified at Willow Creek Mine Unit 10 near the altered sandstone contact (Fig. 14), constraining the pH at the back of the roll to below pH 5. The proportion of marcasite decreases toward the reduced, unaltered contact, and it is absent from the middle of the vertical transect to the barren, reduced border. In addition, a grain collected from heavy separates sampling the middle of the vertical transect showed co-precipitation of ferroselite and barite (Fig. 16). The stability fields of these two mineral phases overlap under higher pH conditions and constrain the pH within the middle of the vertical transect to above 5.4 (Fig. 20). The evidence of marcasite coupled with the barite-ferroselite

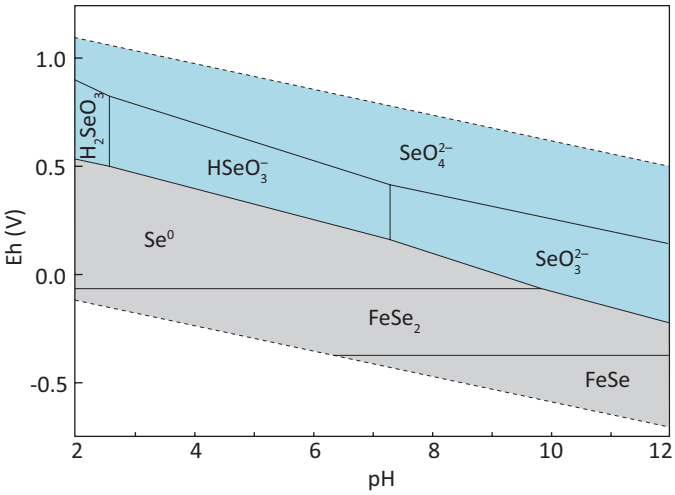

Fig. 19. Eh-pH diagram of solid (gray) and aqueous (blue) selenium phases. Solid black lines indicate equilibrium boundaries between selenium species. Se^0-$FeSe_2$ equilibrium boundary occurs at an Eh just below 0 V. Modeled on Geochemist Workbench 11.0.2: temperature = 25°C, pressure = 1 atm, Fe^{2+} = 10^{-3} M, Se = 10^{-5} M, S = 10^{-3} M (nonselenium-bearing phases suppressed; plot does not include thermodynamic data for Fe-S-Se solid solution). Ionic concentrations were taken from Nye (2015) and cross-referenced with common activities used in calculations by Drever (1997) in natural waters in similar settings.

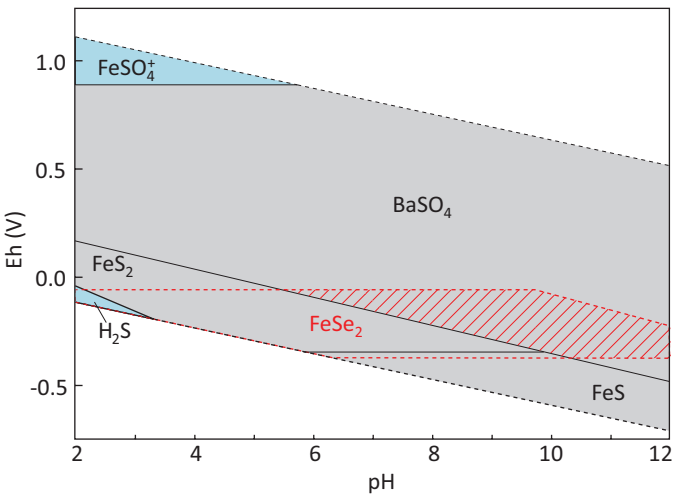

Fig. 20. Eh-pH diagram of Fe-Ba-S system overlain with ferroselite stability field (Fig. 19). Solid sulfur phases indicated in gray; aqueous phases indicated in blue. Ferroselite stability field is outlined on the diagram with the dashed red line. The overlap of barite and ferroselite stability fields is indicated with the red striped zone. This constrains the minimum pH for coprecipitation of barite and ferroselite above 5.4. Modeled on Geochemist Workbench 11.0.2: temperature = 25°C, pressure = 1 atm, Fe^{2+} = 10^{-3} M, Ba^{2+} = 10^{-6} M, S = 10^{-3} M. Ionic concentrations were taken from Nye (2015) and cross-referenced with common activities used in calculations by Drever (1997) in natural waters in similar settings.

constraint indicates, at a minimum, acid neutralization from pH 5 to pH 5.4 across the tail of the roll sampled at Willow Creek Mine Unit 10, in confirmation of abiogenically derived sulfur isotope observations. Biogenic redox was proposed as the dominant mechanism for pyrite recycling and roll-front propagation at Willow Creek Mine Unit 10 because of abundant pyrite and its extensive association with organic material. Trends of $\delta^{34}S$ values from biogenically derived pyrite identified prolific bacterial activity, and Eh/pH gradients interpreted from trends of $\delta^{34}S$ values from abiogenically derived pyrite corroborate chemical conditions expected to be established through biogenic redox. Further mineralogical evidence supports abiogenic isotopic interpretations and, in combination with core observations and biogenic and abiogenic sulfur isotope interpretations, substantiates the prominent role of SRB in the development and advancement of the Willow Creek Mine Unit 10 roll front.

Conclusions

We have identified that both biogenic and abiogenic redox contributed to ore formation at Lost Creek and Willow Creek Mine Unit 10, and we demonstrated that pyrite morphology can be used to distinguish its biogenic or abiogenic mode of formation. This is substantiated by the definitive differences in $\delta^{34}S$ values between morphologic types evident in both deposits examined in this study. Because of the unique controls of biogenic and abiogenic redox processes on sulfur isotope fractionation, differentiating the formation mechanisms allowed us to utilize sulfur isotope trends to assess both bacterial prolificacy and Eh/pH conditions established during ore formation:

1. The Lost Creek deposit propagated through abiogenic pyrite recycling in a buffered solution at near-neutral pH. $\delta^{34}S$ values from biogenically derived pyrite displayed an extreme range, exhibiting Rayleigh fractionation and indicating limited sulfate availability and restricted bacterial activity. The distribution of pyrite across the Lost Creek deposit confirmed abiogenic pyrite recycling as the dominant redox mechanism, with lesser influence from biogenic redox. Sulfur isotope trends from abiogenically derived pyrite indicated that ore precipitation was predominantly driven by an Eh drop across the roll under conditions of buffered, near-neutral pH, as supported by the pervasive appearance of calcite cement.
2. Willow Creek Mine Unit 10 was controlled by biogenic redox evident from the $\delta^{34}S$ values of framboidal pyrite, which indicated rapid bacterial sulfate reduction and prolific bacterial activity. Abiogenic sulfur isotope trends identified decreasing Eh and increasing pH across the roll emulating chemical conditions predicted for biogenic redox. The abiogenic trends were further substantiated by spatial and temporal variations of the Willow Creek Mine Unit 10 ore assemblage, which confirmed Eh/pH gradients with evidence from selenium-bearing phases, marcasite, and the coprecipitation of ferroselite and barite.

The chemical conditions of these deposits strongly influenced the resultant ore assemblages. Willow Creek Mine Unit 10 is dominated by tyuyamunite mineralization and is the consequence of biogenic redox. Lost Creek, which formed through abiogenic redox, contains primarily coffinite, uraninite, and brannerite. This study has applied sulfur isotope analyses to delineate the controls on the chemical conditions governing these roll-front deposits and elucidate the formation mechanisms of the epigenetic mineral assemblages fundamental to deposit characterization. Recent studies of uranium biomineralization (e.g., Bhattacharyya et al., 2017) highlight the importance of biogenic processes in the formation of sandstone-hosted roll-front deposits. This work shows that sulfur isotope data may be used to identify and characterize biogenic processes in this environment. In addition, it highlights the importance of complex, coupled biogenic and abiogenic components in natural roll-front deposits.

Acknowledgments

The authors acknowledge financial support from the University of Wyoming School of Energy Resources and the Department of Geology and Geophysics, and a Natural Sciences and Engineering Research Council (NSERC) Discovery Grant to Fayek. UR Energy and Uranium One provided critical samples and information about the geology of these deposits. Carrick Eggleston (University of Wyoming) and Cal VanHolland (UR Energy) provided valuable discussions and suggestions during the course of this research. We thank Nathaniel Applegate for help with Geochemist Workbench calculations and Ryan Sharp for invaluable assistance during SIMS data acquisition. Finally, we thank two anonymous reviewers and the editors at *Economic Geology* for very thoughtful and helpful suggestions for improvements to the manuscript.

REFERENCES

Abzalov, M.Z., and Paulson, O., 2012, Sandstone hosted uranium deposits of the Great Divide Basin, Wyoming, USA: Applied Earth Science, v. 121, p. 76–83, doi: 10.1179/1743275812Y.0000000017.

Agarwala, U., Rees, C.E., and Thode, H.G., 1965, Sulfur isotope effects in the hydrogen ion decomposition of thiosulfate: Canadian Journal of Chemistry, v. 43, p. 2802–2811, doi: 10.1139/v65-391.

Berner, R.A., 1970, Sedimentary pyrite formation: American Journal of Science, v. 268, p. 1–23, doi: 10.2475/ajs.268.1.1.

——1984, Sedimentary pyrite formation: An update: Geochimica et Cosmochimica Acta, v. 48, p. 605–615, doi: 10.1013/0016-7037(84)90089-9.

Bhattacharyya, A., Campbell, K.M., Kelly, S.D., Roebbart, Y., Weyer, S., Bernier-Latmani R., and Borch, T., 2017, Biogenic non-crystalline U(IV) revealed as major component in uranium ore deposits: Nature Communications, v. 8, article 15538, doi: 10.1038/ncomms15538, 8 p.

Bonnetti, C., Cuney, M., Michels, R., Truche, L., Malartre, F., Liu, X., and Yang, J., 2015, The multiple roles of sulfate-reducing bacteria and Fe-Ti oxides in the genesis of the Bayinwula roll front-type uranium deposit, Erlian Basin, NE China: Economic Geology, v. 110, p. 1059–1081, doi: 10.2113/econgeo.110.4.1059.

Bonnetti, C., Liu, X., Zhaobin, Y., Cuney, M., Michels, R., Malartre, F., Mercadier, J., and Cai, J., 2017, Coupled uranium mineralization and bacterial sulphate reduction for the genesis of the Baxingtu sandstone-hosted U deposit, SW Sangliao Basin, NE China: Ore Geology Reviews, v. 82, p. 108–129, doi: 10.1016/j.oregeorev.2016.11.013.

Brüchert, V., 2004, Physiological and ecological aspects of sulfur isotope fractionation during bacterial sulfate reduction: Geological Society of America, Special Paper 379, p. 1–16.

Brunner, B., and Bernasconi, S.M., 2005, A revised isotope fractionation model for dissimilatory sulfate reduction in sulfate reducing bacteria: Geochimica et Cosmochimica Acta, v. 69, p. 4759–4771, doi: 10.0016/j.gca.2005.04.015.

Bullock, L.A., and Parnell, J., 2017, Selenium and molybdenum enrichment in uranium roll-front deposits of Wyoming and Colorado, USA: Journal of Geochemical Exploration, v. 180, p. 101–122, doi: 10.1016/j.gexplo.2017.06.013.

Cheney, E.S., and Jensen, M.L., 1966, Stable isotope geology of the Gas Hills, Wyoming, uranium district: Economic Geology, v. 61, p. 44–71, doi: 10.2113/gsecongeo.61.1.44.

Drever, J.I., 1997, The geochemistry of natural waters: Surface and groundwater environments, 3rd ed.: Upper Saddle River, New Jersey, Prentice Hall, 436 p.

Farrand, M., 1970, Framboidal sulphides precipitated synthetically: Mineralium Deposita, v. 5, p. 237–247, doi: 10.1007/BF00201990.

Ferrini, V., Fayek, M., De Vito, C., Mignardi, S., and Pignatti, J., 2010, Extreme sulphur isotope fractionation in the deep Cretaceous biosphere: Journal of the Geological Society, v. 167, p. 1009–1018, doi: 10.1144/0016-76492009-161.

Finch, R., and Murakami, T., 1999, Systematics and paragenesis of uranium minerals: Reviews in Mineralogy and Geochemistry, v. 38, p. 91–179.

Goldhaber, M.B., 2003, Sediments, diagenesis, and sedimentary rocks, *in* Holland, H.D., and Turekian, K.K., eds., Treatise on geochemistry, v. 7: Oxford, Elsevier Ltd., p. 257–288.

Goldhaber, M.B., and Kaplan, I.R., 1975, Controls and consequences of sulfate reduction rates in recent marine sediments: Soil Science, v. 119, p. 42–55.

Goldhaber, M.B., Reynolds, R.L., and Rye, R.O., 1978, Origin of a south Texas roll-type uranium deposit: II. Sulfide petrology and sulfur isotope studies: Economic Geology, v. 73, p. 1690–1705.

Gomes, M.L., Fike, D.A., Bergmann, K.D., Jones, C., and Knoll, A.H., 2017, Environmental insights from high-resolution (SIMS) sulfur isotope analyses of sulfides in Proterozoic microbialites with diverse mat textures: Geobiology, v. 16, p. 17–34, doi: 10.1111/gbi.12265.

Granger, H.C., and Warren, C.G., 1969, Unstable sulfur compounds and the origin of roll-type uranium deposits: Economic Geology, v. 64, p. 160–171, doi: 10.2113/gsecongeo.64.2.160.

Habicht, K.S., and Canfield, D.E., 1997, Sulfur isotope fractionation during bacterial sulfate reduction in organic-rich sediments: Geochimica et Cosmochimica Acta, v. 61, p. 5351–5361, doi: 10.1016/S0016-7037(97)00311-6.

Habicht, K.S., Canfield, D.E., and Rethmeier, J., 1998, Sulfur isotope fractionation during bacterial reduction and disproportionation of thiosulfate and sulfite: Geochimica et Cosmochimica Acta, v. 62, p. 2585–2595, doi: 10.1016/S0016-7037(98)00167-7.

Harrison, A.G., and Thode, H.G., 1958, Mechanism of the bacterial reduction of sulphate from isotope fractionation studies: Transactions of the Faraday Society, v. 54, p. 84–92, doi: 10.1039/TF9585400084.

Heller, P.L., McMillan, M.E., and Humphrey, N., 2010, Climate-induced formation of a closed basin: Great Divide Basin, Wyoming: Geological Society of America Bulletin, v. 123, p. 150–157, doi: 10.1130/B30113.1.

Howard, III, J.H., 1977, Geochemistry of selenium: Formation of ferroselite and selenium behavior in the vicinity of oxidizing sulfide and uranium deposits: Geochimica et Cosmochimica Acta, v. 41, p. 1665–1678, doi: 10.1016/0016-7037(77)90176-4.

Ingham, E.S., Cook, N.J., Cliff, J., Ciobanu, C.L., and Huddleston, A., 2014, A combined chemical, isotopic and microstructural study of pyrite from roll-front uranium deposits, Lake Eyre Basin, South Australia: Geochimica et Cosmochimica Acta, v. 125, p. 440–465, doi: 10.1016/j.gca.2013.10.017.

Jensen, M.L., 1958, Sulfur isotopes and the origin of sandstone-type uranium deposits: Economic Geology, v. 53, p. 598–616, doi: 10.2113/gsecongeo.53.5.598.

Johnson, R.K., 2008, Characterizations of uranium occurrences in drill core samples Hazen project 10674, revision 1: Hazen Research, Inc., March 24, 2008, Report for UrEnergy USA, Inc., 41 p.

Johnson, R.K., and Schmidt, R., 2007, Characterization of uranium occurrence in sandstone samples Hazen project 10619: Hazen Research, Inc., August 24, 2007, Report for UrEnergy USA, Inc., 20 p.

Jones, G.E., and Starkey, R.L., 1962, Some necessary conditions for fractionation of stable isotopes of sulfur by *Desulfovibrio desulfuricans*: National Science Foundation, National Science Foundation Symposium, Yale University, New Haven, Connecticut, April 12–14, 1962, Proceedings, p. 61–79.

Kaplan, I.R., and Rittenberg, S.C., 1964, Microbiological fractionation of sulphur isotopes: Journal of General Microbiology, v. 34, p. 195–212.

Kehoe, K., 2018, Wyoming's coal geology: Wyoming State Geological Survey website, www.wsgs.wyo.gov/energy/coal-geology, accessed September 2018.

Kohn, M.J., Riciputi, L.R., Stakes, D., and Orange, D.L., 1998, Sulfur isotope variability in biogenic pyrite: Reflections of heterogeneous bacterial colonization: American Mineralogist, v. 38, p. 1454–1468.

Kribek, B., 1975, The origin of framboidal pyrite as a surface effect of sulphur grains: Mineralium Deposita, v. 10, p. 389–396, doi: 10.1007/BF00207896.

Kuznetsov, S.I., Ivanov, M.V., and Lyalikova, N.N., 1963, Introduction to geological microbiology: International series in the earth sciences [translated from Vvedeniye v Geologicheskuyu Mikrobiologiyu, Academy of Sciences: Moscow, USSR Press, 1962]: New York, McGraw-Hill, 252 p.

Langmuir, D., 1978, Uranium solution-mineral equilibria at low temperatures with applications to sedimentary ore deposits: Geochimica et Cosmochimica Acta, v. 42, p. 547–569, doi: 10.1016/0016-7037(78)90001-7.

Leibold, J., 2013, Geochemistry and mineralogy of the alteration halo associated with the Three Crow roll-front uranium deposit, Nebraska, USA: Ph.D. thesis, Golden, Colorado, Colorado School of Mines, 189 p.

MacLean, L.C.W., Tyliszczak, T., Gilbert, P.U.P.A., Zhou, D., Pray, T.J., Onstott, T.C., and Southam, G., 2008, A high-resolution chemical and structural study of framboidal pyrite formed within a low-temperature bacterial biofilm: Geobiology, v. 6, p. 471–480, doi: 10.1111/j.1472-4669.2008.00174.x.

Meek, A.S., 2014, Sandstone uranium deposits of Nebraska and Colorado: A comparative study: M.S. thesis, Winnipeg, Manitoba, University of Manitoba, 141 p.

Min, M., Chen, J., Wang, J., Wei, G., and Fayek, M., 2005, Mineral paragenesis and textures associated with sandstone-hosted roll-front uranium deposits, NW China: Ore Geology Reviews, v. 26, p. 51–69, doi: 10.1016/j.oregeorev.2004.10.001.

Murowchick, J.B., and Barnes, H.L., 1986, Marcasite precipitation from hydrothermal solutions: Geochimica et Cosmochimica Acta, v. 50, p. 2615–2629.

Nakai, N., and Jensen, M.L., 1964, The kinetic isotope effect in the bacterial reduction and oxidation of sulfur: Geochimica et Cosmochimica Acta, v. 28, p. 1893–1912, doi: 10.1016/0016-7037(64)90136-X.

Nye, C.W., 2015, Reconnaissance characterization of the Willow Creek roll front uranium deposit: M.S. thesis, Laramie, Wyoming, University of Wyoming, 174 p.

Ohmoto, H., 1972, Systematics of sulfur and carbon isotopes in hydrothermal ore deposits: Economic Geology, v. 67, p. 551–578, doi: 10.2113/gsecongeo.67.5.551.

Ohmoto, H., and Goldhaber, M.B., 1997, Sulfur and carbon isotopes, *in* Barnes, H.L., ed., Geochemistry of hydrothermal ore deposits (3rd ed.): New York, John Wiley and Sons, p. 517–611.

Rackley, R.I., 1972, Environment of Wyoming Tertiary uranium deposits: American Association of Petroleum Geologists Bulletin, v. 56, p. 755–774.

Reynolds, R.L., Goldhaber, M.B., and Carpenter, D.J., 1982, Biogenic and nonbiogenic ore-forming processes in the south Texas uranium district: Evidence from the Panna Maria deposit: Economic Geology, v. 77, p. 541–556, doi: 10.2113/gsecongeo.77.3.541.

Riciputi, L.R., Paterson, B.A., and Ripperdan, R.L., 1998, Measurement of light stable isotope rations by SIMS: Matrix effects for oxygen, carbon, and sulfur isotopes in minerals: International Journal for Mass Spectrometry, v. 178, p. 81–112.

Rye, R.O., Bethke, P.M., and Wasserman, M.D., 1992, The stable isotope geochemistry of acid sulfate alteration: Economic Geology, v. 87, p. 225–262, doi: 10.2113/gsecongeo.87.2.225.

Sakai, H., 1957, Fractionation of sulphur isotopes in nature: Geochimica et Cosmochimica Acta, v. 12, p. 150–169, doi: 10.1016/0016-7037(57)90025-X.

——1968, Isotopic properties of sulfur compounds in hydrothermal processes: Geochemical Journal, v. 2, p. 29–49.

Sawlowicz, Z., 1993, Pyrite framboids and their development: A new conceptual mechanism: Geologische Rundschau, v. 82, p. 148–156, doi: 10.1007/BF00563277.

Seal, II, R.R., 2006, Sulfur isotope geochemistry of sulfide minerals: Reviews in Mineralogy and Geochemistry, v. 61, p. 633–677, doi: 10.2138/rmg.2006.61.12.

Seal, II, R.R., Alpers, C.N., and Rye, R.O., 2000, Stable isotope systematics of sulfate minerals: Reviews in Mineralogy and Geochemistry, v. 40, p. 541–602, doi: 10.2138/rmg.2000.40.12.

Sharp, W.N., and Gibbons, A.B., 1964, Geology and uranium deposits of the southern part of the Powder River Basin, Wyoming: U.S. Geological Survey, Bulletin 1147-D, 60 p.

Sharpe, R., 2013, The geochemistry and geochronology of the Bong uranium deposit, Thelon Basin, Nunavut, Canada: M.S. thesis, Winnipeg, Manitoba, University of Manitoba, 214 p.

Sharpe, R., and Fayek, M., 2016, Mass bias corrections for U-Pb isotopic analysis by secondary ion mass spectrometry: Implications for U-Pb dating of uraninite: Rapid Communications in Mass Spectrometry, v. 30, p. 1601–1611, doi: 10.1002/rcm.7595.

Stewart, C.L., Reimann, L.J., and Swapp, S., 2000, Mineralogic considerations for uranium in situ leach mining: A preliminary study of uranium and associated mineralogy of roll-front uranium deposits in Wyoming and Nebraska: Canadian Institute of Mining, Metallurgy and Petroleum Bulletin, v. 93, p. 89–96.

Swapp, S.M., 2012, Uranium mineralization and ore-forming processes at Lost Creek: Presentation of Results for UrEnergy USA, Inc., Laramie, University of Wyoming, May 29, 2012.

Veeramani, H., Scheinost, A.C., Monsegue, N., Qafoku, N.P., Kukkadapu, R., Newville, M., Lanzirotti, A., Pruden, A., Murayama, M., and Hochella, Jr., M.F., 2013, Abiotic reductive immobilization of U(VI) by biogenic mackinawite: Environmental Science and Technology, v. 47, p. 2361–2369, doi: 10.1021/es304025x.

Warren, C.G., 1972, Sulfur isotopes as a clue to the genetic geochemistry of a roll-type uranium deposit: Economic Geology, v. 67, p. 759–767, doi: 10.2113/gsecongeo.67.6.759.

Whipkey, C.E., Cavaroc, V.V., and Flores, R.M., 1991, Uplift of the Bighorn Mountains, Wyoming and Montana—a sandstone provenance study: U.S. Geological Survey, Bulletin 1917-D, 28 p.

Whitney, D.L., and Evans, B.W., 2010, Abbreviations for names of rock-forming minerals: American Mineralogist, v. 95, p. 185–187.

Wilkin, R.T., and Barnes, H.L., 1997, Pyrite formation in an anoxic estuarine basin: American Journal of Science, v. 297, p. 620–650.

Zhil'tsova, I., Shmariovich, E.M., Polupanova, L.I., and Perlina, S.A., 1982, Physiochemical conditions of formation of carnotite ore mineralization: Lithology and Mineral Resources, v. 17, p. 515–525.

Zhil'tsova, I.G., Perlina, S.A., and Shmariovich, E.M., 1990, Physical-chemical settings of uranyl vanadate ore formation: Lithology and Mineral Resources, v. 24, p. 350–355.

Gretchen Hough completed research on this project during her M.S. program at the University of Wyoming under the tutelage of Drs. Susan Swapp and Carol Frost. She took an unusual route to graduate school, serving first as a U.S. Peace Corps volunteer teacher in Namibia after earning her undergraduate degree. While she was working toward her M.S. degree, Gretchen completed two internships with Marathon Oil and was hired full time after graduation. However, Gretchen is passionate about science education, and she has stepped back from her career in petroleum geology to pursue a teaching certification for high school sciences in Washington.